actuators

MDPI

Article

Integrated Control of EV Battery Chargers for Virtual Inertia and Vehicle-to-Grid Support Using Hybrid Energy Storage

Chandra Babu Guttikonda [1], Pinni Srinivasa Varma [1], Malligunta Kiran Kumar [1], K. V. Govardhan Rao [2], Joon Ho Choi [3,*], E. Shiva Prasad [4] and Ch. Rami Reddy [4,5,*]

[1] Department of Electrical and Electronics Engineering, Koneru Lakshmaiah Education Foundation, Guntur 522502, India; 2302060001@kluniversity.in (C.B.G.); pinnivarma@kluniversity.in (P.S.V.); mkkumar@kluniversity.in (M.K.K.)
[2] Department of Electrical and Electronics Engineering, St. Martin's Engineering College, Secunderabad 500100, India; govardhaneee@smec.ac.in
[3] Department of Electrical Engineering, Chonnam National University, Gwangju 61186, Republic of Korea
[4] Department of Electrical and Electronics Engineering, VNR Vignana Jyothi Institute of Engineering and Technology, Hyderabad 500090, India; shivaprasad_e@vnrvjiet.in
[5] Applied Science Research Center, Applied Science Private University, Amman 11937, Jordan
* Correspondence: joono@chonnam.ac.kr (J.H.C.); ramireddy_ch@vnrvjiet.in (C.R.R.)

Abstract

The increasing penetration of renewable energy sources and converter-interfaced loads has intensified the need for fast and reliable grid-support services. Although electric vehicle (EV) battery chargers have emerged as promising resources for Vehicle-to-Grid (V2G) applications, existing solutions typically focus on individual services such as virtual inertia or frequency regulation, while limited attention has been given to the coordinated provision of multiple ancillary services within a unified framework. Furthermore, the use of batteries alone for fast frequency support may accelerate battery degradation due to frequent high-power transients. To address these challenges, this paper proposes a hybrid energy storage-based EV battery charger architecture and a coordinated multi-timescale control strategy capable of simultaneously providing virtual inertia support, long-term frequency regulation, reactive power compensation, and harmonic mitigation. The proposed approach utilizes a DC-link capacitor to deliver fast inertial response while the battery supplies sustained frequency support, thereby reducing battery stress and improving energy management efficiency. An enhanced frequency estimation method based on a phase-locked loop combined with a low-pass filter is also introduced to improve dynamic performance. Simulation results demonstrate the effectiveness of the proposed strategy under various grid disturbances. The system achieves an equivalent virtual inertia constant of approximately 1.85 s and delivers up to 786 W of transient inertial support within 80 ms during frequency events. The enhanced frequency estimation method significantly reduces transient overshoot, while harmonic compensation limits the grid current and voltage total harmonic distortion to 1.50% and 3.23%, respectively. In addition, the controller provides up to 400 VAR of reactive power support during voltage disturbances while maintaining stable battery operation. These results demonstrate that the proposed EV battery charger can function as a multifunctional grid-support resource, enhancing frequency stability, voltage regulation, power quality, and overall V2G capability in future smart grids.

Keywords: EV battery chargers; DC-DC converter; hybrid energy storage; dual converter; total harmonic distortion

Check for updates

Academic Editors: Mohamad Alzayed and Hicham Chaoui

Received: 10 May 2026
Revised: 12 June 2026
Accepted: 14 June 2026
Published: 19 June 2026

Copyright: © 2026 by the authors. Licensee MDPI, Basel, Switzerland. This article is an open access article distributed under the terms and conditions of the Creative Commons Attribution (CC BY) license.

1. Introduction

As the global transition toward renewable energy accelerates, power systems face increasing challenges in maintaining frequency stability due to the declining presence of synchronous generators and the associated mechanical inertia. To address this issue, the concept of Grid-Forming and Grid-Following Virtual Inertia (GFL VI) has emerged as a critical solution. This paper presents a comprehensive study on the implementation of GFL VI in Electric Vehicle Battery Chargers (EVBCs) using a novel control strategy [1,2]. The approach leverages a hybrid energy storage system (HESS) composed of a DC-link capacitor and a battery to emulate virtual inertia and provide full Vehicle-to-Grid (V2G) functionality, including long-term frequency support, voltage regulation through reactive power compensation, and harmonic current filtering [3,4]. A two-stage AC–DC converter topology is proposed, integrating a three-phase Voltage Source Inverter (VSI) and a Dual Active Bridge (DAB) resonant DC–DC converter to interface with the grid and the EV battery, respectively. The control architecture is modular, incorporating fast, medium, and slow dynamic controllers to manage different timescale requirements efficiently [5–7]. Key innovations include an enhanced frequency estimation method using a phase-locked loop (PLL) with a low-pass filter (LPF) to minimize overshoot and improve transient response, and the strategic management of energy flow between the capacitor and battery to preserve battery life while ensuring rapid frequency response [8,9]. Most renewable energy systems are connected to the grid through inertialess power electronics converters, leading to a decrease in the overall system inertia and consequently to deviations of frequency beyond the acceptable range, resulting in undesirable load-shedding or even large-scale blackouts [10].

These frequency variations can be quantified by two parameters, the time derivative of the frequency, known as rate-of-change-of-frequency (ROCOF), and the minimum value of the frequency during the transient period, known as frequency nadir [11–14], which are shown in Figure 1. To overcome this problem, researchers have proposed the concept of virtual inertia (VI) [15] which consists of the integration of an energy storage system (ESS) into the grid to emulate the synchronous generator behavior [16,17] by grid-connected converters (GCCs), commonly called grid-forming converters (GFMs) [17–20]. However, since GCCs with GFM control strategies are controlled as a voltage source, the direct control of the AC voltage without an inner current control loop may lead to difficulties in dealing with voltage drop faults, generating over currents and stability problems, making these solutions challenging to integrate into distribution grids [21].

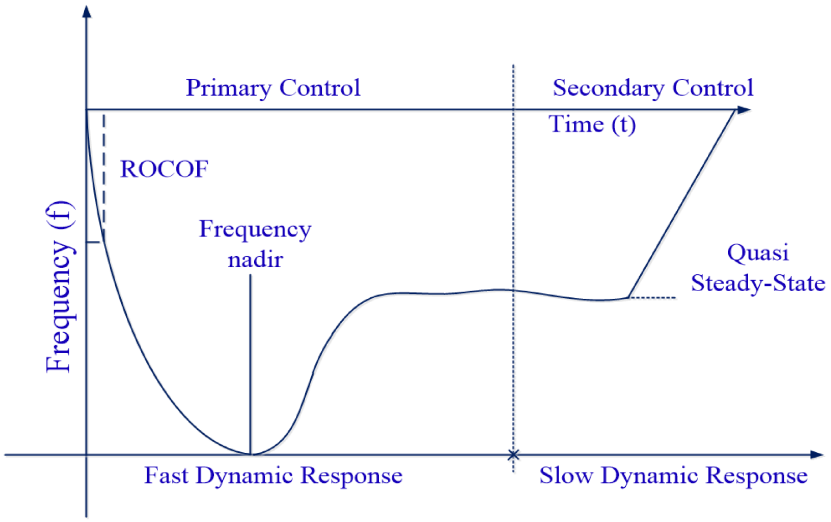


Figure 1. Transient response of grid frequency.

The proposed control strategy is validated through both analytical modeling and simulation results, demonstrating its efficacy in delivering robust frequency and voltage support under grid disturbances. This work offers a scalable, firmware-based upgrade path for existing EVBCs, supporting their role as active participants in modern, flexible power systems. Table 1 provides literature survey data on HESS technology.

In Table 1, existing studies primarily focus on hybrid energy storage configurations, energy management strategies, and renewable energy integration. However, limited attention has been given to the coordinated implementation of virtual inertia, long-term frequency regulation, reactive power support, and harmonic compensation within a unified EV battery charger architecture. Furthermore, most existing approaches either rely solely on DC-link capacitors for inertia emulation or employ hybrid energy storage systems without integrating comprehensive V2G ancillary services. To address these gaps, this work proposes a dual-converter EV battery charger equipped with a hybrid energy storage system and a multi-timescale control framework capable of delivering full V2G functionality while improving frequency stability, voltage support, and power quality.

The structure of the paper is organized into several key sections. It begins with the Abstract, providing a concise summary of the objectives, methodology, and findings of the study. The Introduction follows, highlighting the challenges posed by reduced system inertia due to renewable energy integration and introducing the concept of virtual inertia using EV battery chargers with a hybrid energy storage system (HESS). A literature review presents related work on HESS technologies, control strategies, and applications, summarizing gaps addressed by the proposed method. The Fundamentals of GFL Virtual Inertia section explains the theoretical basis, mathematical modeling, and limitations of conventional GFL VI implementations. The Proposed Control Strategy section outlines the two-stage power converter architecture and details the multi-timescale control scheme, dividing it into fast (AC current), medium (DC-link voltage, VI, battery current), and slow (power and droop) response controllers, along with enhanced PLL-based frequency estimation. The Simulation Results section validates the effectiveness of the proposed system through tests on harmonic compensation, virtual inertia performance, HESS dynamic response, and voltage support under different grid events. Finally, the Conclusion summarizes the benefits of the proposed strategy, including improved frequency stability, better harmonic performance, and enhanced suitability for future V2G applications, supported by a brief comparison with existing works and a comprehensive References section.

The main contribution of the paper is the development of a smart control strategy for Electric Vehicle Battery Chargers (EVBCs) that helps support the power grid by providing virtual inertia, frequency regulation, voltage support, and harmonic compensation. This is achieved using a hybrid energy storage system (HESS) that combines a fast-responding DC-link capacitor and a slower battery, allowing for efficient energy management. The paper introduces a two-stage converter system and designs a multi-level control scheme with fast, medium, and slow response times. It also improves frequency estimation by using a phase-locked loop (PLL) with a low-pass filter to reduce overshoot. Simulation results show that the proposed system can handle sudden changes in grid frequency, reduce power distortion, and support voltage during sags, making it a practical and scalable solution for enhancing the stability and flexibility of modern power grids through existing EV infrastructure.

Table 1. Literature survey on hybrid energy storage systems.

Ref.	Title & Authors	Focus Area	Key Contributions	Applications	Challenges/ Future Work
[22]	Abo-Khalil et al. (2023)—*Advancements and Challenges in HESS*	Topologies, control strategies, integration	Overview of ESS types, control techniques (e.g., MPC, fuzzy, SMC), design considerations	Renewable grids, microgrids	Standardization, interdisciplinary integration, reliability
[23]	Babu et al. (2020)—*Comprehensive Review of HESS*	Converter control strategies	Classification of HESS control methods (rule-based, fuzzy, predictive), limitations	Standalone/grid-connected microgrids	Unified control design, real-time validation
[24]	Schubert et al. (2023)—*HESS with Redox-Flow Batteries*	RFB-based HESS, EMS optimization	KPIs for battery–supercapacitor–RFB hybrids, optimal EMS designs	Stationary storage, grid applications	Advanced EMS algorithms, better RFB coupling
[25]	Cholidis et al. (2025)—*Optimized Storage for Ports*	HRES, EMS, GA-based optimization	Renewable-powered port energy systems, 54% cost reduction using HESS + EMS	Smart ports, maritime energy	Empirical EMS design, grid backup strategies
[26]	Reddy & Kumar (2024)—*HESS for EV Drive Systems*	EV power systems, control architecture	Feedback control circuit to isolate battery from regenerative braking	Electric vehicles (EVs)	Reducing EV energy loss, improving battery lifespan
[27,28]	Jiao (2022)—*HESS Capacity Optimization and LCA*	Optimization, environmental impact	LPF-based control to minimize capacity oversizing; LCA of HESS	100% RES integration	Environmental trade-offs, lifecycle emissions
[28]	Adeyinka et al. (2024)—*HESS for Grid Integration*	Grid stability and HESS	Review of HESS integration with variable renewables	Grid-connected RES	Demand forecasting, inverter coordination
[29]	Punyavathi et al. (2024)—*LEV Power Management with ML*	ML-based HESS control	ML ensures precise voltage, torque, and speed regulation	Light electric vehicles (LEVs)	Integration of AI into real-time drive control
Proposed	---	Virtual inertia, V2G support, HESS management, dual-converter architecture	Proposes a multi-timescale control strategy integrating virtual inertia, long-term frequency regulation, reactive power compensation, and harmonic mitigation using a HESS consisting of a DC-link capacitor and EV battery; introduces enhanced PLL-LPF-based frequency estimation and coordinated energy management through VSI–DAB converter architecture	Smart grids, V2G-enabled EV charging stations, renewable-rich distribution networks, ancillary grid services	Experimental validation under hardware implementation, scalability assessment for large EV fleets, cyber-secure V2G communication, and real-time field deployment

Research Gap and Motivation

Despite significant advances in virtual inertia control, hybrid energy storage systems, and Vehicle-to-Grid technologies, several important challenges remain unresolved. Existing virtual inertia implementations commonly rely on either DC-link capacitors or battery energy storage systems alone. While DC-link capacitors can provide fast inertial response, their limited energy capacity restricts their ability to sustain grid-support services for extended periods. Conversely, battery-based inertia support can supply larger amounts of energy but may accelerate battery degradation due to frequent charge–discharge cycles associated with rapid frequency disturbances. Furthermore, most reported studies focus on a single ancillary service, such as virtual inertia or frequency regulation, without considering the simultaneous provision of reactive power support and harmonic compensation. In addition, coordinated energy management strategies capable of effectively distributing fast and slow dynamic responses among different storage elements remain limited.

Therefore, there exists a need for an integrated EV battery charger architecture that can simultaneously provide fast virtual inertia support, long-term frequency regulation, reactive power compensation, and harmonic mitigation while minimizing battery stress and improving overall grid-support capability. To address these challenges, this work proposes a hybrid energy storage-based EV battery charger employing a coordinated multi-timescale control framework in which the DC-link capacitor supplies rapid transient support and the battery delivers sustained energy support. The proposed approach enables comprehensive V2G functionality while enhancing grid stability, power quality, and energy management performance.

The main contributions of this work are summarized as follows:

1. Development of a dual-converter EV battery charger architecture incorporating a hybrid energy storage system composed of a DC-link capacitor and battery.
2. Design of a multi-timescale control framework that decouples fast virtual inertia support from long-term frequency regulation.
3. Implementation of coordinated active and reactive power control for simultaneous frequency support and voltage regulation.
4. Integration of harmonic compensation functionality to improve power quality at the grid interface.
5. Validation of the proposed strategy through comprehensive simulation studies under frequency disturbances, voltage variations, and harmonic conditions.

2. Fundamentals of GFL VI

The GFL VI concept is based on the dynamics of the swing equation which is given by (1):

$$p_g - p_l = \Delta p = 2H\frac{d}{dt}\Delta f_{pu} \quad (1)$$

where

$\frac{d}{dt}$—derivative of time;
Δf_{pu}—frequency deviation;
Δp—power difference for generated power and load power;
H—inertia constant.

It can be easily followed that for a certain variation in power, inertia reduction in power systems leads to higher ROCOF and higher peak deviation of frequency. Hence, the

concept of GLF VI consists of the integration of ESS for adding extra power to the system according to (2):

$$p_g - p_l + p_{support} = \Delta p + p_{support} = 2H\frac{d}{dt}\Delta f'_{pu} \quad (2)$$

$$p_{support} - 2H_v\frac{d}{dt}\Delta f'_{pu} \quad (3)$$

where $\Delta f'_{pu}$ is the instantaneous frequency of the system.

Then, substituting (3) into (2), the frequency dynamics of the system including the VI are given by the following:

$$\Delta p = 2(H + H_V)\frac{d}{dt}\Delta f'_{pu} = 2H'\frac{d}{dt}\Delta f'_{pu} \quad (4)$$

This way, the effective inertia constant is increased to $H' = H + H_V$, increasing the frequency stability.

The implementation of the GFL VI approach in a VSI was introduced according to the functional diagram presented in Figure 2. Note that the GFL VI approach relates the frequency deviation Δf_{PLL}, measured by PLL, with a voltage deviation ΔV_{DC}, in the DC-link voltage, according to a gain K_ω. Moreover, the control strategy considers the well-known voltage and current control loops as presented in the block diagram of Figure 3.

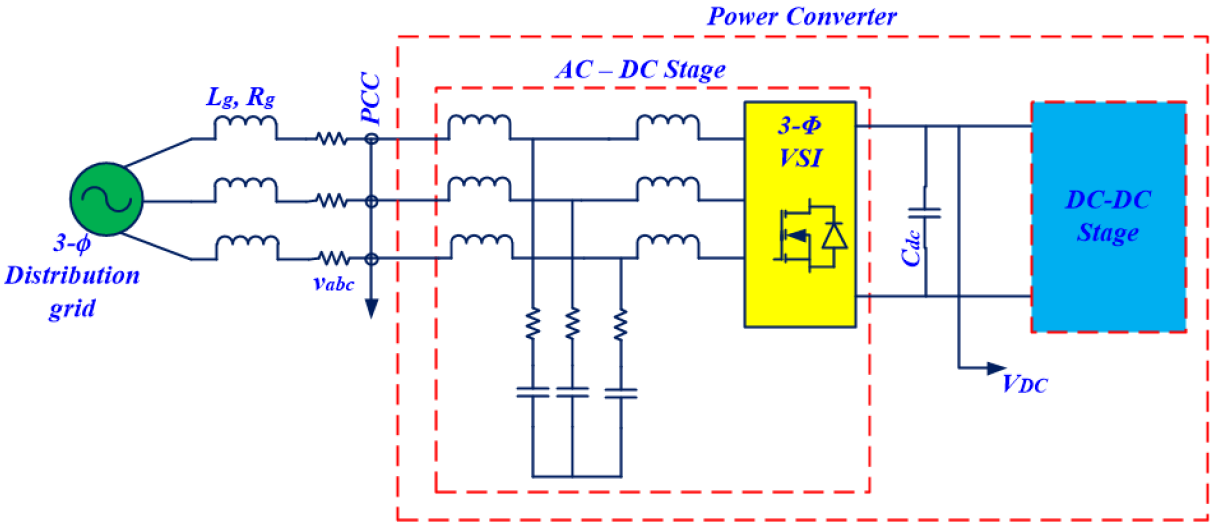


Figure 2. Traditional GFL VI implementation in a VSI.

Hence, a frequency deviation, Δf_{PLL}, generates a fast response of power through releasing/storing the energy in the DC-link capacitor CDC according to a "virtual inertia" (Hv) coefficient given by (5):

$$H_V = K_\omega H_C \quad (5)$$

$$H_C = \frac{C_{DC}\ V_{ref}^2}{2\ P_o} \quad (6)$$

where

C_{DC}—capacitance;
V_{ref}—rated voltage in DC link;
P_o—nominal power

The gain K_ω in (5) is designed for the allowed maximum frequency deviation Δf_{max} and a maximum voltage variation ΔV_{DC_max} according to (7), where f_b and V_{ref} are the base grid frequency and the rated DC bus voltage, respectively:

$$K_\omega = \frac{\Delta V_{DC\_max}}{\Delta f_{max}} \frac{f_b}{V_{ref}} \tag{7}$$

Then, the dynamic response of DC-link voltage is related to the fast power response ΔP_{DC} (inertia response) according to the following:

$$\Delta P_{DC}(s) \approx \frac{2H_V P_o}{f_b} \underbrace{s\Delta f_{PLL}(s)}_{R_o C_o F} \tag{8}$$

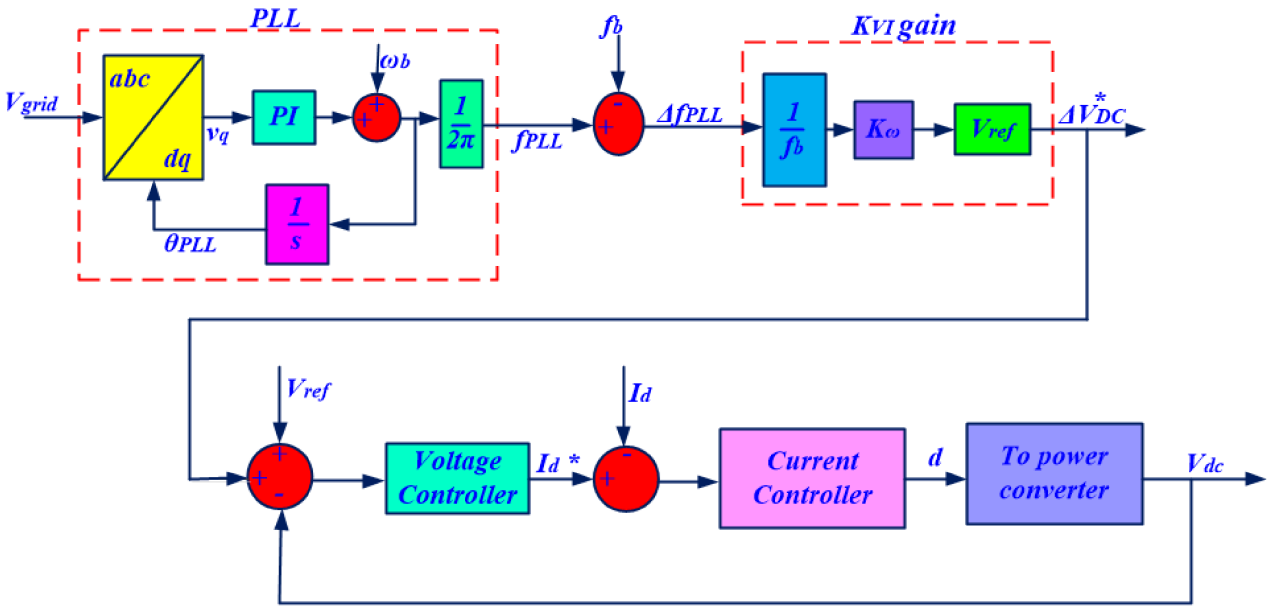


Figure 3. Typical GFL VI control strategy.

3. Measurement Limitations to Implementing GFL VI

3.1. Power Constraints for VI Supply

For a correct design of the converter, the extra power ΔP_{DC} for VI implementation must be considered as an overload. For instance, the relation between overloading capability ΔP_{DC}, ROCOF and different inertia values is given in (8), considering a base frequency of 60 Hz. Note that for a ROCOF of 2 Hz/s and an inertia contribution of $H_V \approx 3.75$ s, an overloading capability of 25% is required. Moreover, considering $H_V = 5$ s, for a ROCOF of 2 Hz/s, 33% of overloading capability is required. Whereas, for a ROCOF of 4 Hz/s and a $H_V = 5$ s, the required overload is 66%. Hence, GFL VI implementation supporting high values of inertia and faster ROCOF constraints requires oversizing the AC–DC converter, which will increase the size and price of EVBCs.

3.2. Frequency Measurement from PLL

To analyze the influence of the PLL dynamic in VI power response, the block diagram of the frequency estimation of a typical second-order PLL, as shown in Figure 4, is considered.

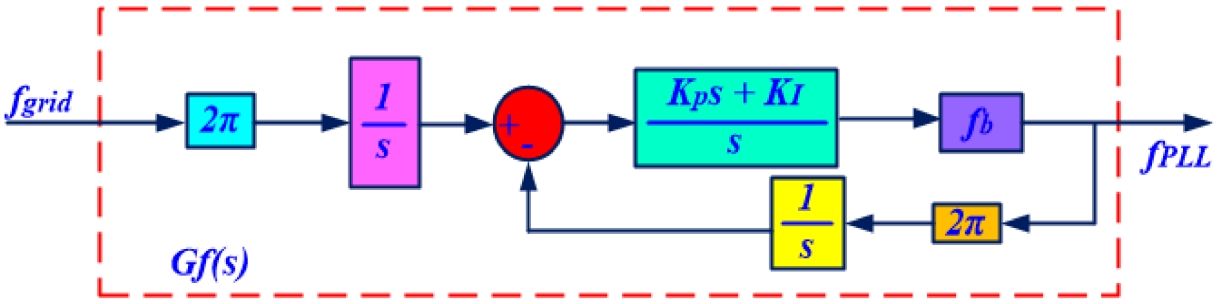


Figure 4. Frequency estimation dynamic by PLL.

Where f_b is the grid frequency, while K_p and K_I are, respectively, the proportional and integral gains of the PI controller. Therefore, the closed-loop $G_f(s)$ transfer function (TF) for frequency estimation can be expressed by the following:

$$G_f(s) = \frac{f_{PLL}}{f_{grid}} = \frac{\omega_b K_p s + \omega_b K_I}{s^2 + \omega_b K_p s + \omega_b K_I} \tag{9}$$

The controller gains are then tuned. The K_p gain is calculated to achieve the desired bandwidth ω_{bw} and the integral gain is tuned at $K_I = K_p \frac{\omega_{bw}}{10}$. Then, with the evaluation $G_{fCL}(s)$ for a unit ramp $f_{grid}(s) = \frac{1}{s^2}$, the ROCOF is calculated according to the following:

$$R_o C_o F(s) = s f_{PLL}(s) = \frac{\omega_{bw} s + 0.1\,\omega_{bw}^2}{s^2 + \omega_{bw} s + 0.1\,\omega_{bw}^2} \frac{1}{s} \tag{10}$$

Thus, the maximum value of estimated ROCOF by PLL is 1.07 Hz/s. This means an overshoot of 7% that, according to (8), increases the transient peak power supplied by the converter ΔP_{DC}. To overcome the above-mentioned issues, an enhanced design procedure along with a novel control strategy to implement VI, long-term frequency support, reactive power support, and harmonics correction is introduced in the following sections.

4. Proposed Control Strategy

The block diagram of the proposed control strategy and the scheme of the power stage are shown in Figure 5. Note that a two-stage AC–DC topology is adopted which is composed of a three-phase VSI to interface with the grid, and a Ddual Active Bridge series resonant DC–DC converter to interface with the EV battery.

In the proposed control strategy, different V2G functionalities are implemented through managing a HESS as shown in Figure 6. For this purpose, six controllers are designed: the AC current controller, the DC bus voltage controller, the DC current controller, the VI controller, the PQ controllers (active power P and reactive power Q controllers), and the droop controllers to compensate for frequency and voltage variations. In addition, a computational block to calculate active and reactive power (PQ block), a PLL, and transformation blocks complete the control strategy. The management of HESS allows to decouple the dynamics responses of active power as shown in Figure 6. Note that in front of a frequency variation increment Δf_{PLL}, the power delivered by the converter P_g is given by the following:

$$P_g = P_c + P_{EV} \tag{11}$$

where P_c and P_{EV} are active powers supplied by the DC-link capacitors and the EV battery, respectively. The power P_c has a faster dynamic response compared to P_{EV}, and it is intended for VI support unlike P_{EV} which is focused on long-term frequency support. For simplicity, no power losses are considered. Moreover, in the proposed control strategy, the controllers are classified according to timescale as fast, medium, and slow response. A fast response is required for the inner AC current controller on the AC–DC stage, with a timescale of around a few milliseconds. The medium response is related to DC-link voltage, VI, and DC current control, with a timescale of several milliseconds. Finally, the slow response corresponds to the PQ and droop controller with a timescale of several seconds. Since special care must be taken in choosing the bandwidth of medium response controllers to ensure system stability, the transfer functions and controller design are explained as follows.

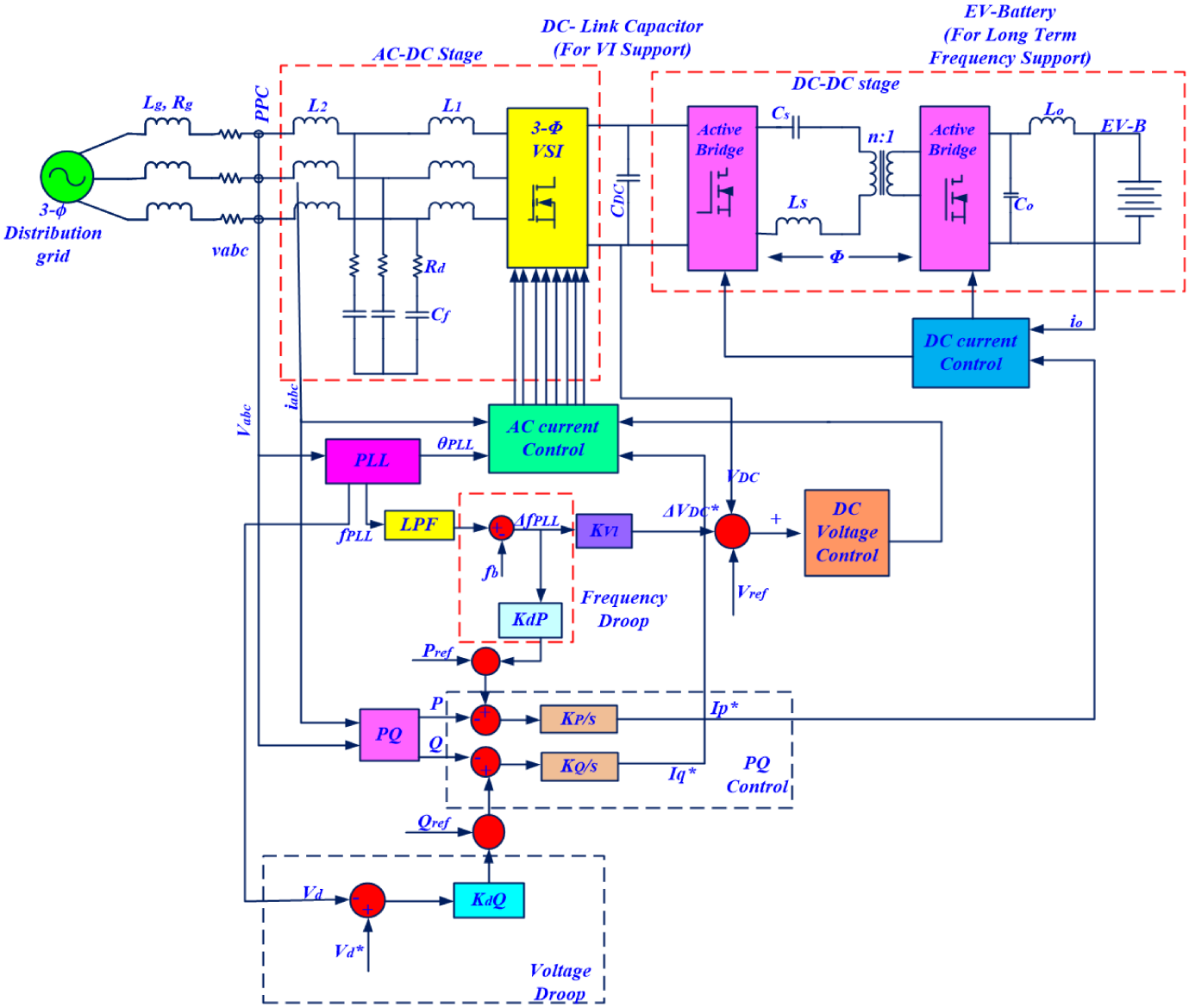


Figure 5. Block diagram of control strategy for V2G support in EVBCs.

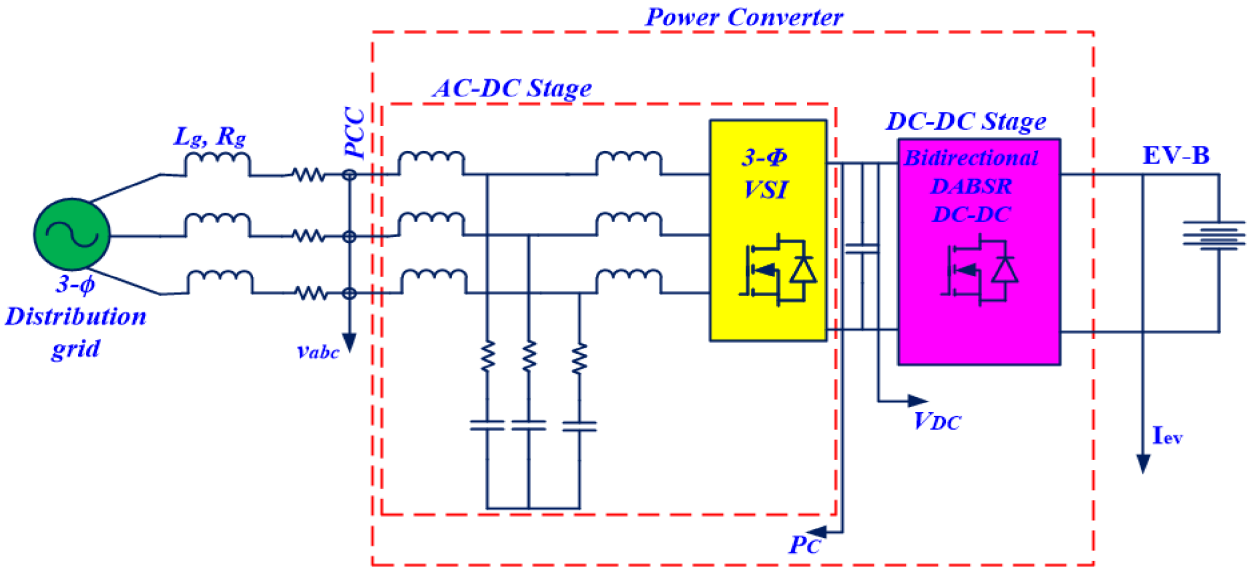


Figure 6. Block diagram of the proposed HESS management.

4.1. Stability Analysis of the Proposed Control Strategy

The proposed EVBC-HESS controller adopts a hierarchical multi-timescale control architecture in which the individual control loops operate at different bandwidths. Such a design is widely used in power electronic systems to ensure dynamic decoupling and stable operation.

The AC current controller is designed as the fastest loop with a bandwidth of approximately 800 Hz, enabling rapid current tracking and disturbance rejection. The PLL and DC-link voltage controller operate at intermediate bandwidths of approximately 60 Hz and 30 Hz, respectively, while the battery current controller and active/reactive power controllers operate at slower timescales ranging from 5 Hz to 1 Hz. This bandwidth hierarchy ensures that the inner loops reach steady-state conditions before the outer loops respond, thereby minimizing dynamic interactions among controllers.

The ratio between adjacent control bandwidths is maintained above two, providing sufficient dynamic separation and reducing the possibility of control-loop coupling. In addition, the low-pass filter integrated into the frequency estimation mechanism suppresses high-frequency measurement noise and mitigates transient overshoot, thereby improving system damping characteristics.

The stability of the proposed framework is further verified through simulation studies under frequency disturbances of ± 0.2 Hz, voltage variations of 17 V, and ROCOF conditions up to 3 Hz/s. In all cases, the system exhibits stable responses without sustained oscillations, divergence, or controller saturation. The DC-link voltage, battery current, and active/reactive power outputs remain within acceptable operating limits throughout the disturbances, confirming the effectiveness of the proposed control architecture.

Therefore, the combination of bandwidth separation, hierarchical control design, and coordinated energy management contributes to the stable operation of the proposed EVBC-HESS under a wide range of operating conditions.

4.2. Fast Response Control: The AC Current Controller

For AC current, proportional + resonant controllers in the stationary $\alpha\beta$ frame are adopted. The TF from VSI voltage to AC current is given by (12) where L_1, L_2, C_f *and* R_d

are respectively the VSI side inductance, grid side inductance, filter capacitance, and damping resistance [29]:

$$G_{iv} = \frac{i_\alpha(s)}{v_\alpha(s)} = \frac{R_d C_f s + 1}{C_f L_1 L_2 s^3 + R_d C_f (L_1 + L_2) s^2 + (L_1 + L_2) s} \quad (12)$$

The transfer function of the PR controllers with selective harmonic GPR(s) is defined in (13), where KP_c is the proportional gain, Kr_j (j = 13,57,9) are the gains for resonant components, and the term ξ is the damping factor which defines the bandwidth of the resonant components and the gain at each resonance frequency:

$$G_{PR}(s) = K_{PC} + \sum_{j-1}^{n} \frac{Kr_j s}{s^2 + 2\,\xi\omega_o s + \omega_o^2} \quad (13)$$

4.3. Medium Response Control

4.3.1. DC-Link Voltage Controller

The DC-link voltage controller is designed to provide the reference I_{d_ref} for the AC current controller according to the following equation:

$$G_{vi}(s) = \frac{v_{DC}(s)}{i_d\,(s)} \approx m\,\frac{1}{C_{DC} s}\mathrm{C} \quad (14)$$

where m is the modulation index.

Moreover, since the reference for the DC-link voltage ΔV_{DC}^* is provided by the VI controller, the dynamics of the VI controller should be slower to ensure the system stability.

4.3.2. Enhanced GFL VI Controller

As explained in the discussion on limitations of GFL VI, the traditional GFL VI approach generates an overshoot of 7% in the frequency estimation by the PLL. To reduce the overshoot, the estimated frequency f_{PLL} is filtered by a first-order low-pass filter (LPF), as shown in Figure 6. The LPF must be tuned with a cutoff frequency lower than the DC-link voltage dynamic response to ensure stability. To evaluate the effectiveness on the resulting overshoot, the PLL response was evaluated with three different configurations: a PLL tuned at 10 Hz bandwidth without LPF, a PLL tuned at 60 Hz bandwidth without LPF, and a PLL tuned at 60 Hz bandwidth with an LPF tuned at 10 Hz. The PLL with LPF overshoot value can be obtained by evaluating the PLL TF $G_f(s)$, given by (9), including the LPF TF, leading to the following:

$$ROCOF(s) = \frac{\omega_{bw}(s) + 0.1\,\omega_{bw}^2}{s^2 + \omega_{bw} s + 0.1\,\omega_{bw}^2} \frac{1}{s} \left(\frac{\frac{\omega_{bw}}{6}}{s + \frac{\omega_{bw}}{6}} \right) \quad (15)$$

With cutoff frequency of $\frac{\omega_{bw}}{6}$ for the LPF, following the procedure-detailed frequency measurement from PLL, a maximum ROCOF of 1.004 Hz/s is calculated. Hence, the overshoot in the estimated frequency has been considerably decreased, which leads lower transient peak deviation for both DC bus voltage and supplied power for VI.

4.3.3. Battery Current Controller

The equivalent circuit to control battery current I_o is shown in Figures 7 and 8, where L_0, C_0 are the inductance and capacitance for the DC filter and R_0 is the inductor series resistance, whereas the averaged current source $\left\langle i_{ohf} \right\rangle$ is given by the following:

$$\left\langle i_{oh\,f} \right\rangle = \frac{8\,n\,V_{DC}}{\pi^2 Z\left(F - \frac{1}{F}\right)} \sin(\varnothing) \tag{16}$$

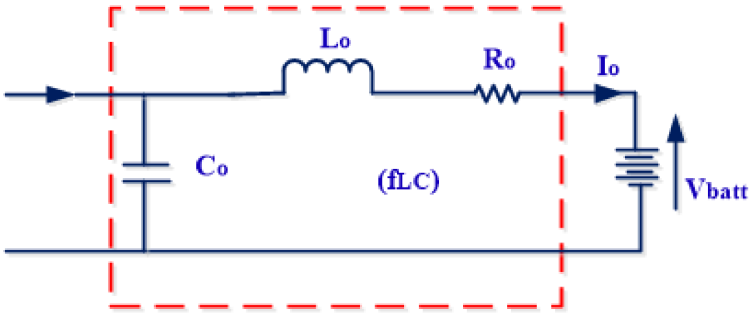


Figure 7. Battery current equivalent circuit.

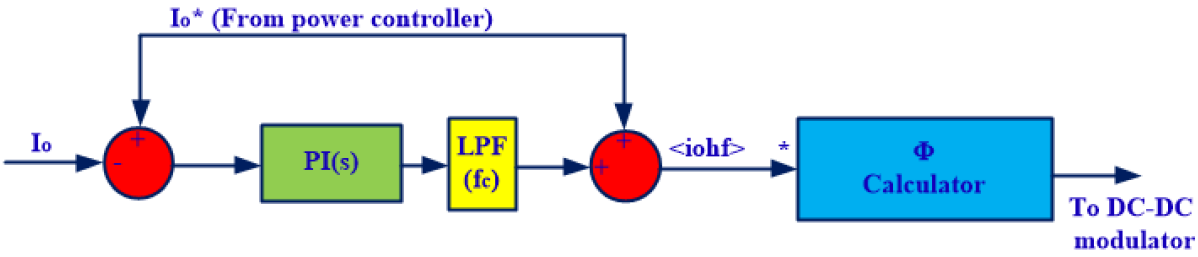


Figure 8. Battery current controller circuit.

In (16), φ is the phase-shift angle, n is the turns ratio of HF transformer, V_{DC} is the DC-link voltage, Z is the tank impedance, and F is the ratio between the switching frequency ω_s and the resonance frequency ω_r. The parameters Z, F, and ω_r are defined in (17), where L_s and C_s are the inductance and capacitance of the resonant circuit:

$$Z = \sqrt{\frac{L_s}{C_s}}\ ;\ F = \frac{\omega_s}{\omega_r}\ ;\ \omega_r = \frac{1}{\sqrt{L_s C_s}} \tag{17}$$

Then, according to Figure 7, the simplified TF for battery current I_0 is given by the following equation:

$$G_i = \frac{I_o\,(s)}{\left\langle i_{oh\,f} \right\rangle (s)} = \frac{\omega_{LC}^2}{s^2 + \frac{R_o}{L_o} s + \omega_{LC}^2} \tag{18}$$

where ω_{LC} is the cutoff frequency of the L_0, C_0 filter.

The block diagram of the proposed DC current controller is shown in Figure 8. The LPF is tuned at ω_c considering two decades lower than ω_{LC} to attenuate the resonance peak of $G_i(s)$. With this consideration, the loop-gain TF (T_i) can be approximated according to (19), where $G_{i0}(s)$ is considered as unity since $\omega_c \ll \omega_{Lc}$. Then, the zero ω_i is tuned to eliminate the pole. Thus, the closed-loop TF $G_{iCL}(S)$ is given by (20):

$$G_{iOL} = PI(s)LPF(s)G_{io}(s) = k_p \left(\frac{s + \frac{1}{T_i}}{s}\right) \frac{\omega_c}{(s + \omega_c)} \tag{19}$$

$$G_{iCL} = \frac{G_{iOL}}{1 + G_{i\_OL}} = \frac{k_p \omega_c}{(s + k_p \omega_c)} \tag{20}$$

4.3.4. Slow Response Controller

Instantaneous values of active power p and reactive power q are computed in the synchronous dq frame according to the following equations:

$$p = \frac{3}{2}(v_d i_d + v_q i_q) \tag{21}$$

$$q = \frac{3}{2}(v_d i_q - v_q i_q) \tag{22}$$

Since v_q is tracked by PLL synchronization, $v_q \approx 0$ and $v_d \, v_m$, where V_m is the amplitude of grid voltages. Therefore, TFs for p and q are given by the following:

$$G_{pq}(s) = \frac{p}{i_d}(s) = \frac{q}{i_q}(s) = \frac{3}{2}V_m \tag{23}$$

Then, integral controllers with gains K_p, K_q are adopted from Figure 5 and the closed-loop TFs G_{pcL}, G_{qcL} are given by the following:

$$G_{pcL}(s) = G_{qcL}(s) = \frac{1.5\, V_m\, K_p}{s + 1.5\, V_m K_p} = \frac{1.5\, V_m\, K_q}{s + 1.5\, V_m K_q} \tag{24}$$

Finally, droop controllers are tuned through gains K_{dP} and K_{dQ}, according to the following equations:

$$P^* = P_{ref} + K_{dP}\, \Delta f_{PLL} \tag{25}$$

$$Q^* = Q_{ref} + K_{d\,Q}(V_d^* - v_d) \tag{26}$$

5. Validation of the Control Strategy

To validate the proposed control strategy, a MATLAB 2026a simulation is developed based on the parameters listed in Table 2. For this ΔV_{DCmax} is limited to ensure the limited modulation, whereas the DC-link capacitance is sized considering the maximum allowed extra power ΔP_{max} for VI support. Therefore, ΔP_{DC}, given by (8), must be limited to ΔP_{max}, according to the following equation:

$$\Delta P(s) \approx \frac{2\, H_V\, P_O}{f_b} R_o C_o F_{max} \leq \Delta P_{max} \tag{27}$$

Then, from (6), (7), and (27), the maximum allowable DC capacitance is calculated by the following:

$$C_{DC} \leq \frac{f_b\, \Delta\, P_{max}}{K_\omega\, V_{ref}^2\, R_o C_o F_{max}} \tag{28}$$

Since $\mathrm{ROCOF_{max}}$ is an a priori known value defined by grid codes, the gain K_ω, given by (7), is calculated as K_ω = 17.65 from parameters of Table 2. Then, replacing values in (28), $C_{DC} \leq 3.13$ mF is calculated. With this consideration, C_{DC} = 2.9 mF is adopted. Then, according to (5) and (6), an inertia of $HV \approx 1.85$ is obtained; thus, the converter can provide VI in front of frequency variations up to 3 Hz/s without exceeding its limits. On the other side, according to constraints in the proposed control strategy, the chosen controller's bandwidths are listed in Table 3.

Table 2. Parameters of the EVBC simulation model.

Parameter	Variable	Value
Rated Power	$P_0 \pm \Delta P_{max}$	2.5 kW ± 500 W
Grid Frequency	$f_b \pm \Delta f_{max}$	60 Hz ± 0.2 Hz
DC-Link Voltage	$V_{ref} \pm \Delta V_{DCmax}$	425 V ± 25 V
Grid Voltage	$V_m \pm \Delta V_m$	179 ± 17 V_p
Max. Considered ROCOF	$ROCOF_{max}$	3 Hz/s
Battery Voltage	V_b	400 V
DAB Switching Frequency	f_{sDC}	100 kHz
VSI Switching Frequency	f_{sAC}	48 kHz
LCL Filter	L_1, L_2, C_f *and* R_d	900 µH, 250 µH, 15 µF and 2 Ω
Tank Impedance	C_r, L_r	10.2 nF, 300 µH
Transformer Turns Ratio	n_t	1
Battery Filter	L_0, C_0, R_0	300 µH, 16 µF, 0.2 Ω
DC- Link Capacitance	C_{DC}	2.9 mF

Table 3. Bandwidths for the controller.

Fast		Medium			Slow
AC Current	PLL	Bus DC	Frequency LPF	Battery Current	P & Q
800 Hz	60 Hz	30 Hz	10 Hz	5 Hz	1 Hz

Note in Table 3 that the controllers are classified according to the dynamic response. The AC current controller is the fastest, whereas the active and reactive controllers (P&Q) are the slowest. Moreover, among the medium dynamic response controllers, the PLL is tuned considering a bandwidth equal to the grid frequency [9], whereas the DC-link voltage controller has a bandwidth higher than the battery current and the LPF cascaded to the PLL, which ensures the stability of the system [30]. Hence, considering the bandwidths of Table 2, the controller parameters are listed in Table 4.

Table 4. Controller gains of the EVBC.

Controller	Gains
AC Current	$K_{pc} = 5.3$, $K_{ic} = 2668$, $K_{r3} = 889$, $K_{r5} = 533$, $K_{r7} = 381$, $K_{r9} = 296$
Battery Current	$K_{pbc} = 1$, $K_{lbc} = 31.416$
PLL	$K_{ppll} = 1$, $K_{ipll} = 37.7$
DC-Link Voltage	$K_{pv} = 0.6489$, $K_{iv} = 4.8036$
Inertia	$K_{VI} = 125$
Droop	$K_{dp} = 2000$, $K_{dq} = 23.53$
P—Q Controller	$K_p = 0.0234$

The PLL, DC-link voltage, and AC current controller parameters are tuned following the methodology of a grid-connected converter. The battery current and P&Q controllers' parameters are calculated according the first-order systems given by (20) and (24), respectively, and the desired bandwidth given in Table 3. Finally, the droop gains K_{dP} and K_{dQ} are calculated considering power deviations of $\Delta P_{ref} = 400$ W and $\Delta PQ_{ref} = 400$ VAR for frequency and voltage variations of 0.2 Hz and 17 V, respectively.

5.1. Stability and Robustness Considerations

The proposed control strategy employs a multi-timescale architecture in which the control loops are designed with well-separated bandwidths to reduce dynamic coupling and improve system stability. As shown in Table 3, the AC current controller operates with the highest bandwidth (800 Hz), followed by the PLL (60 Hz), DC-link voltage controller (30 Hz), low-pass filter (10 Hz), battery current controller (5 Hz), and active/reactive power controllers (1 Hz). This hierarchical arrangement ensures that faster loops reach steady-state operation before slower loops respond, thereby minimizing adverse interactions among the controllers.

The stability of the proposed framework can be qualitatively justified through the adopted bandwidth separation. The ratio between adjacent control bandwidths exceeds a factor of two, which is commonly employed in cascaded power electronic control systems to guarantee stable operation and sufficient dynamic decoupling. In addition, the LPF integrated with the PLL reduces frequency estimation overshoot and prevents oscillatory responses during transient grid events.

To assess robustness, the proposed system was subjected to several operating disturbances, including frequency variations of ± 0.2 Hz, voltage amplitude reductions of 17 V, and ROCOF conditions up to 3 Hz/s. Under all tested conditions, the system maintained stable operation without sustained oscillations, controller saturation, or instability. The DC-link voltage remained within its designed operating range, the battery current remained properly regulated, and the active/reactive power support functions operated as intended.

These results indicate that the proposed multi-timescale control framework possesses satisfactory robustness against practical grid disturbances and parameter variations. Future work will focus on developing a detailed small-signal state-space model and performing eigenvalue, gain-margin, and phase-margin analyses to further quantify the stability characteristics of the proposed EVBC-HESS.

5.2. Dynamic Reactive Power Support Performance

To further evaluate the effectiveness of the proposed control strategy, a reactive power reference variation test was conducted. In this scenario, the reactive power reference was changed from 0 VAR to +400 VAR and subsequently returned to 0 VAR while the active power support and virtual inertia functions remained operational.

The results show that the reactive power controller successfully tracks the commanded reference with a fast transient response and negligible steady-state error. During the transition, the active power support function remained unaffected, demonstrating effective decoupling between active and reactive power control loops. In addition, the DC-link voltage remained within its operating limits and the battery current exhibited minimal variation, indicating that the reactive power compensation function does not impose significant additional stress on the energy storage system.

These observations confirm that the proposed EVBC-HESS architecture can reliably provide dynamic reactive power support while simultaneously maintaining frequency support and virtual inertia services. Therefore, the controller is suitable for practical grid-support applications where reactive power requirements may vary continuously due to changing load and network conditions.

6. Simulation Results

6.1. Harmonic Compensation

To test this functionality, the converter was connected to an AC grid with THDv = 3.19%. The corresponding voltage harmonic spectrum is presented in Figure 9. The test was performed considering a load of 1.6 kW (64% of the rated power). The resulting AC is presented

in Figures 10 and 11. Note that the main harmonics components of grid current and voltage have been suppressed and the obtained THD is only 1.50% and 3.23% respectively.

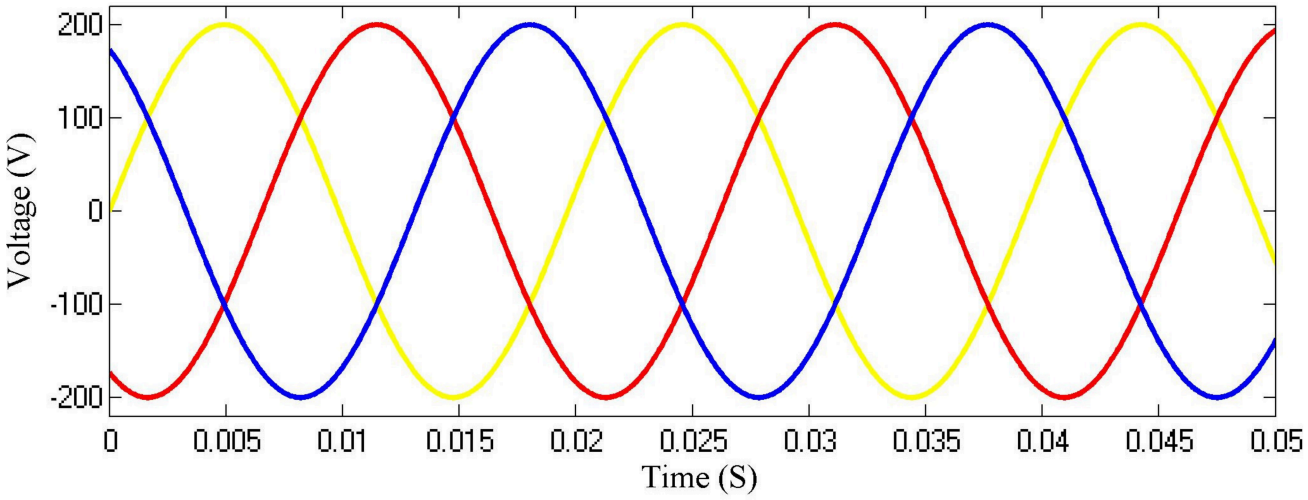


Figure 9. Grid voltage waveform.

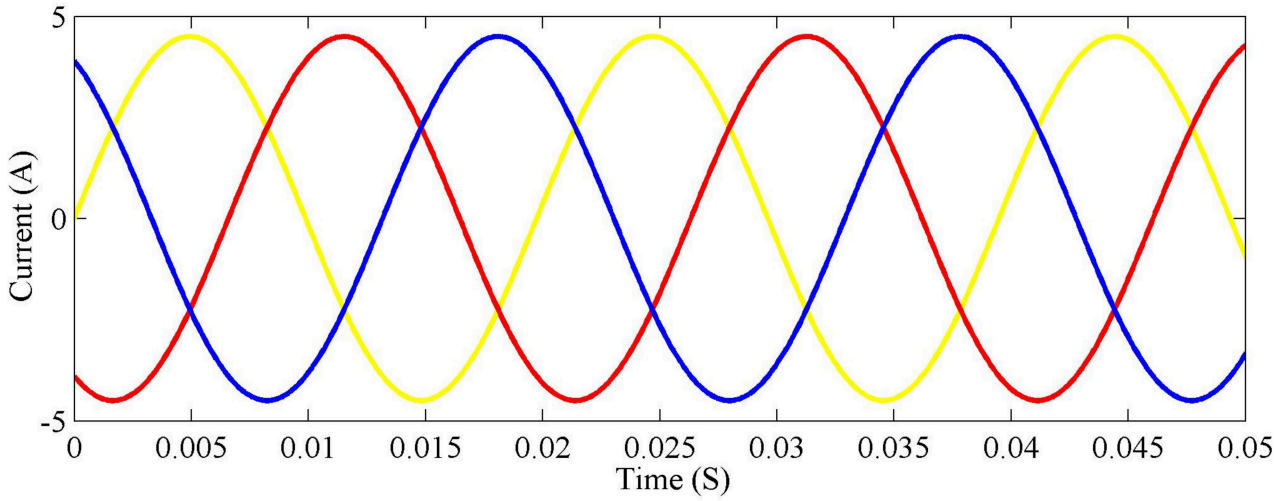


Figure 10. Grid current waveform.

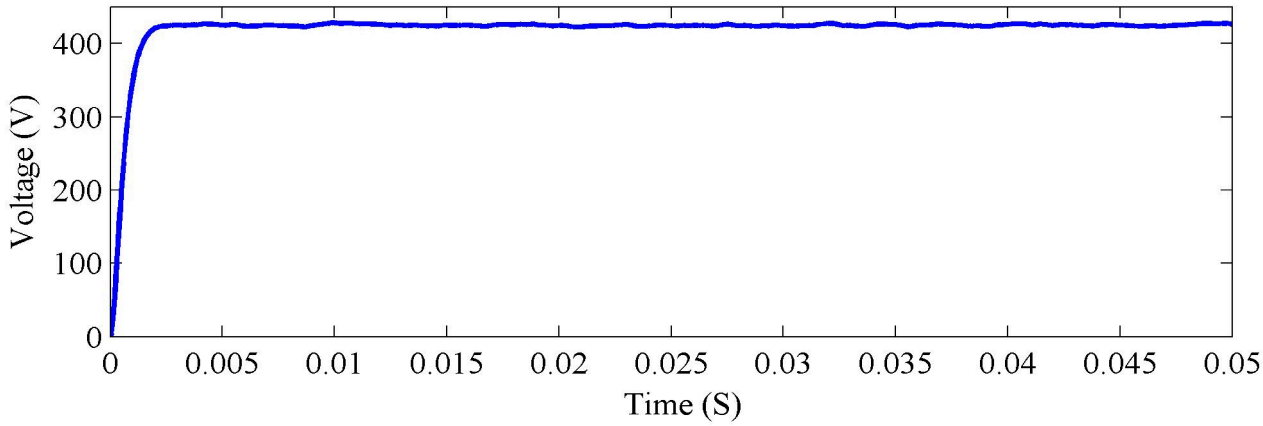


Figure 11. Compensated voltage waveform.

Figures 12 and 13 present the Fast Fourier Transform (FFT) analysis of the grid current and voltage waveforms after the application of the proposed harmonic compensation strat-

egy. The harmonic spectra demonstrate that the dominant low-order harmonic components are significantly attenuated through the action of the proportional–resonant controller and selective harmonic compensation loops.

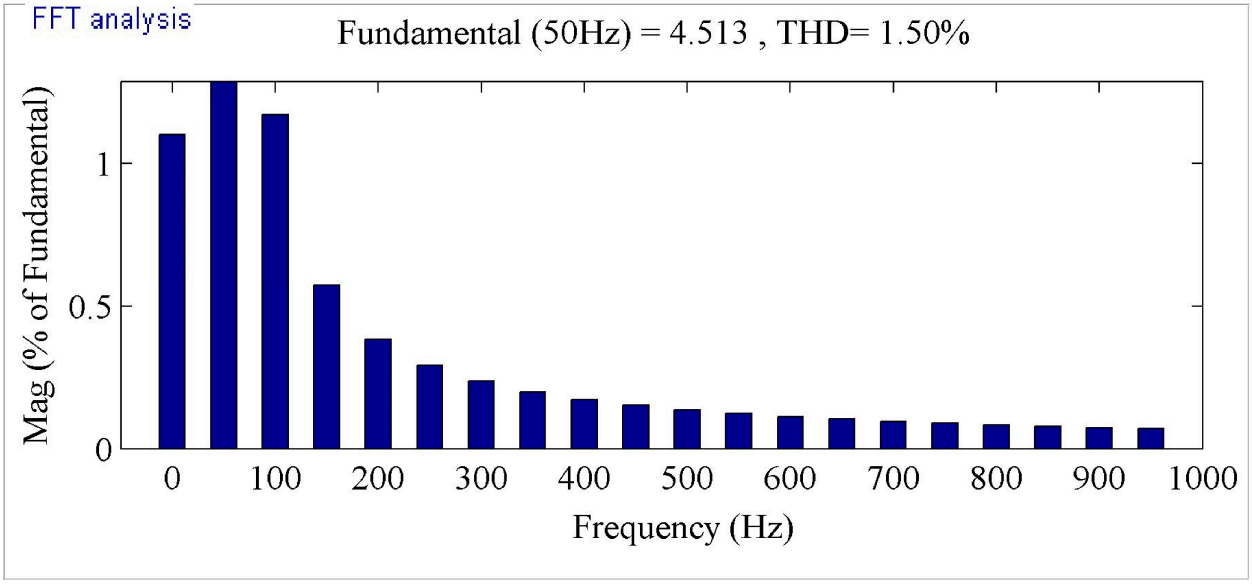


Figure 12. FFT spectrum of compensated grid current showing suppression of dominant low-order harmonics and a resulting THD of 1.50%.

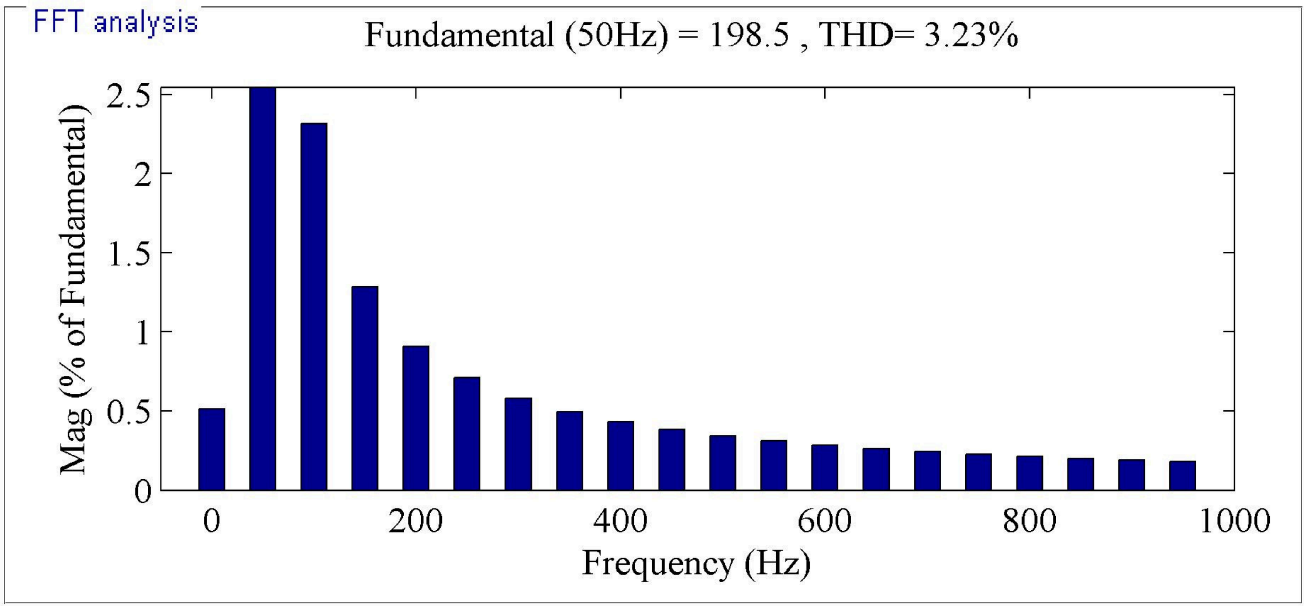


Figure 13. FFT spectrum of compensated grid voltage demonstrating improved voltage quality with a THD of 3.23% after harmonic compensation.

From Figure 12, the grid current exhibits a total harmonic distortion (THD) of approximately 1.50%, which is well below the limits recommended by IEEE 519 standards for grid-connected power electronic systems. The suppression of the third, fifth, seventh, and ninth harmonic components confirms the effectiveness of the resonant control structure in tracking sinusoidal reference currents and mitigating harmonic injection into the utility grid.

Similarly, Figure 13 illustrates the FFT spectrum of the compensated grid voltage. The voltage THD is maintained at approximately 3.23%, indicating improved voltage quality at

the point of common coupling. The results confirm that the proposed control framework not only provides virtual inertia and frequency support but also contributes to power quality enhancement through harmonic mitigation.

6.2. Enhanced VI Response

The dynamic response of the estimated frequency for a frequency step of 0.2 Hz is shown in Figure 14. Two cases are analyzed to estimate the grid frequency: using only a PLL and using a PLL cascaded to a first-order LPF. The bandwidth of the PLL is 60 Hz, whereas for the LPF it is 10 Hz. Then filtering the estimated frequency with an LPF allows to decrease the overshoot considerably which validates the analytic and simulation results of the proposed method shown in Figure 8.

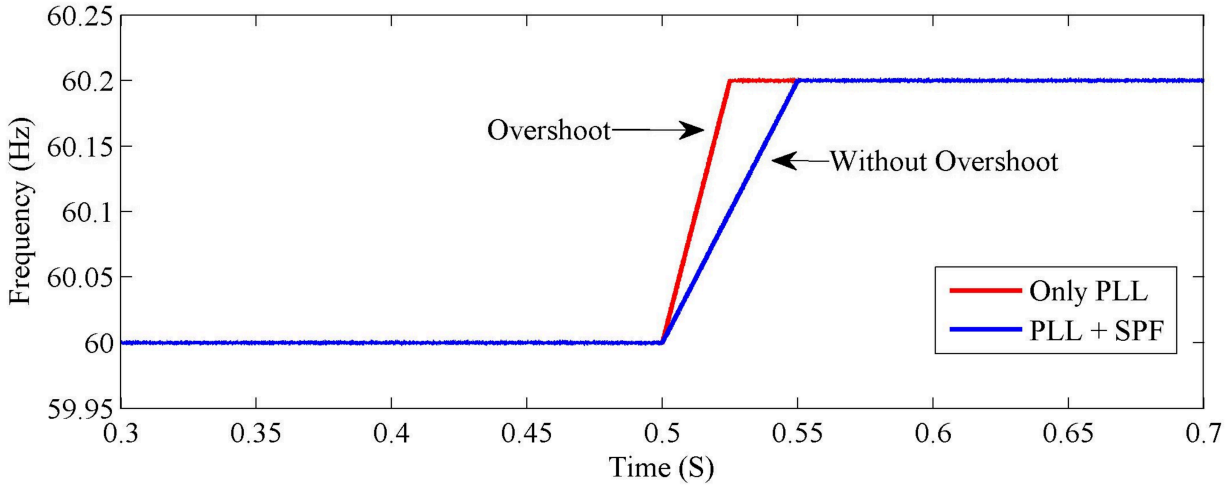


Figure 14. Dynamic response of estimated frequency.

The VI response was validated for "grid to vehicle" (G2V) mode at 1.1 kW. For this test, the droop controllers were disabled. The resulting waveforms are shown in Figures 15 and 16, respectively. For a step-up frequency variation of +0.2 Hz, the measured RoCoF was 5.1 Hz/s. As frequency increases, DC voltage reference is increased proportionally to gain K_{VI} from 425 to 450 V. The DC-link capacitor current achieves a transient peak value of 3.6 A, increasing the grid current to 3 A. The fast dynamic response of active power for VI support achieves a transient peak of 786 W, according to (8), returning to the steady state of −1.1 kW after 80 ms. Note that the current consumed by the battery remains almost constant at 2.56 A but presents a little variation caused by DC-link voltage change. The obtained results are coherent with the estimations, where VI support is supplied by the DC-link capacitors, maintaining the battery current almost constant.

6.3. HESS Response in Front of Frequency Steps

The full control strategy was verified by a frequency step event of ±0.2 Hz in Figures 17 and 18, respectively. In Figure 17 the EVBC initially extracts 1.1 Kw from the grid, working in G2V mode. The measured frequency by PLL is 60 Hz, the grid current peak value is 4.09 A, DC-link voltage takes its nominal value of 425 V, and the battery current is 2.56 A. Then, a frequency step of +0.2 Hz is applied.

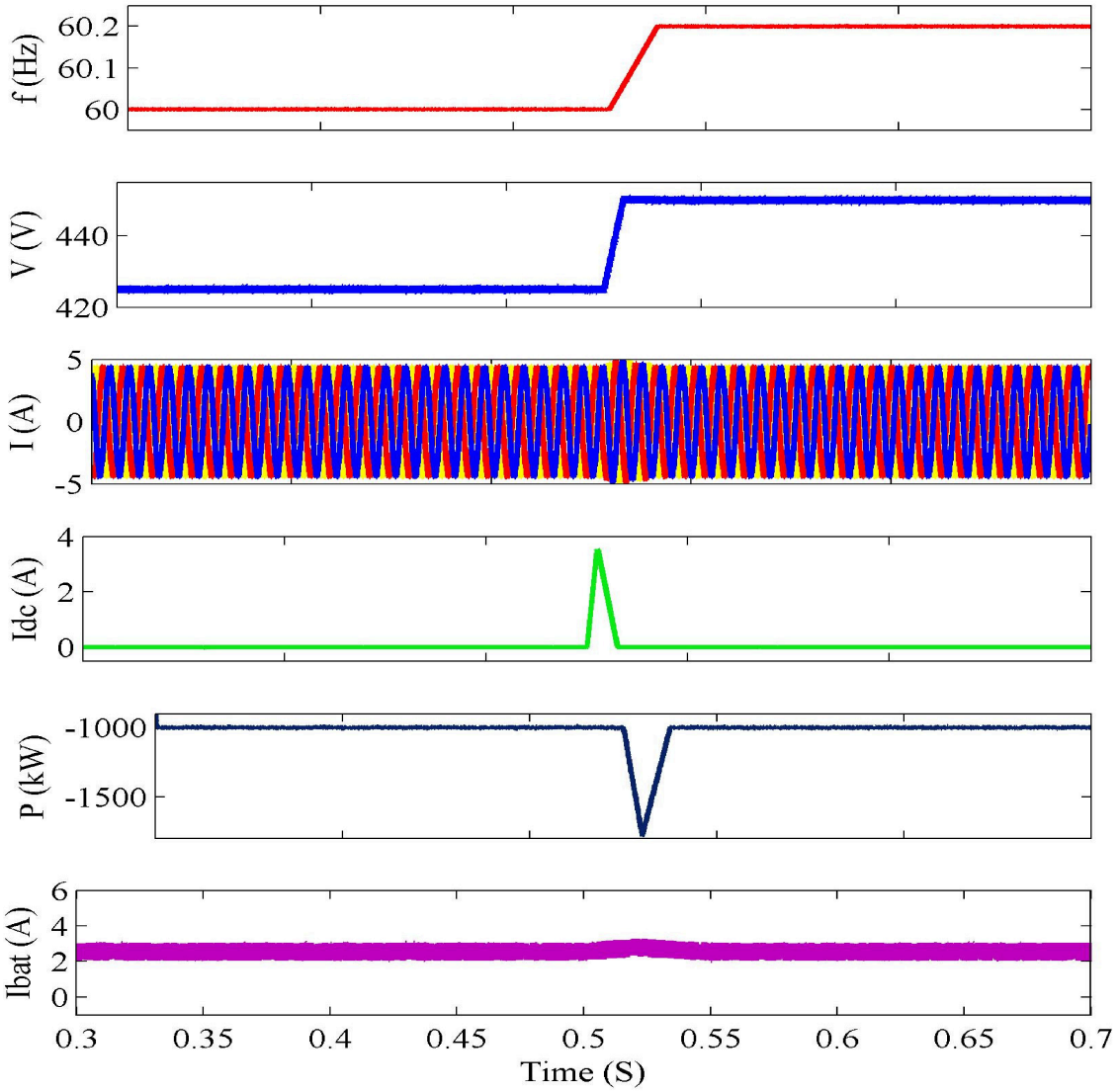


Figure 15. Waveforms for frequency variation of +0.2 Hz.

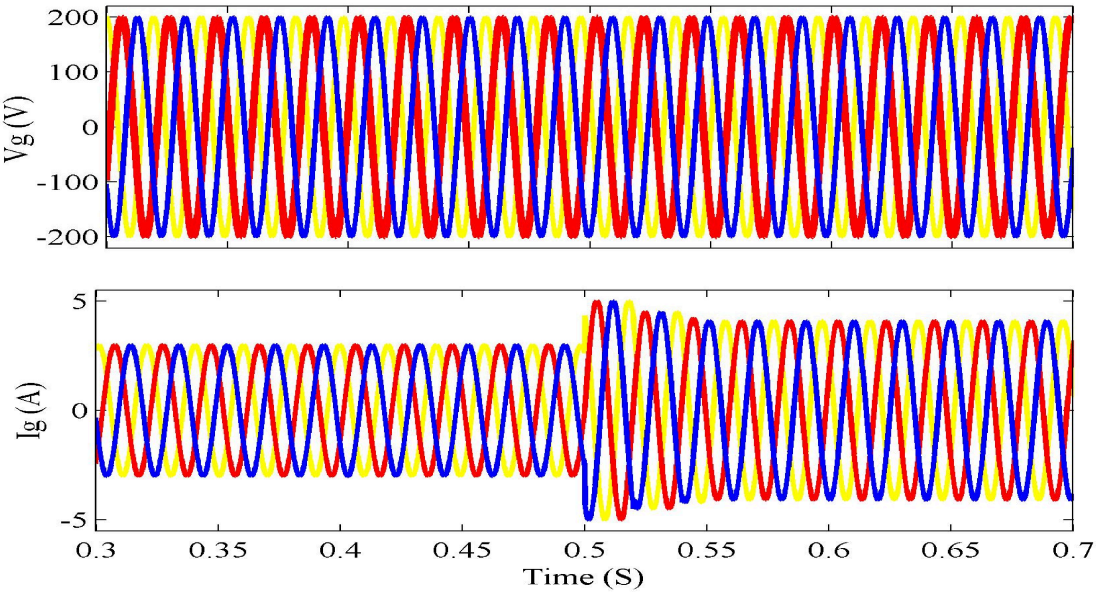


Figure 16. Waveforms of grid voltage and currents for a frequency variation of +0.2 Hz.

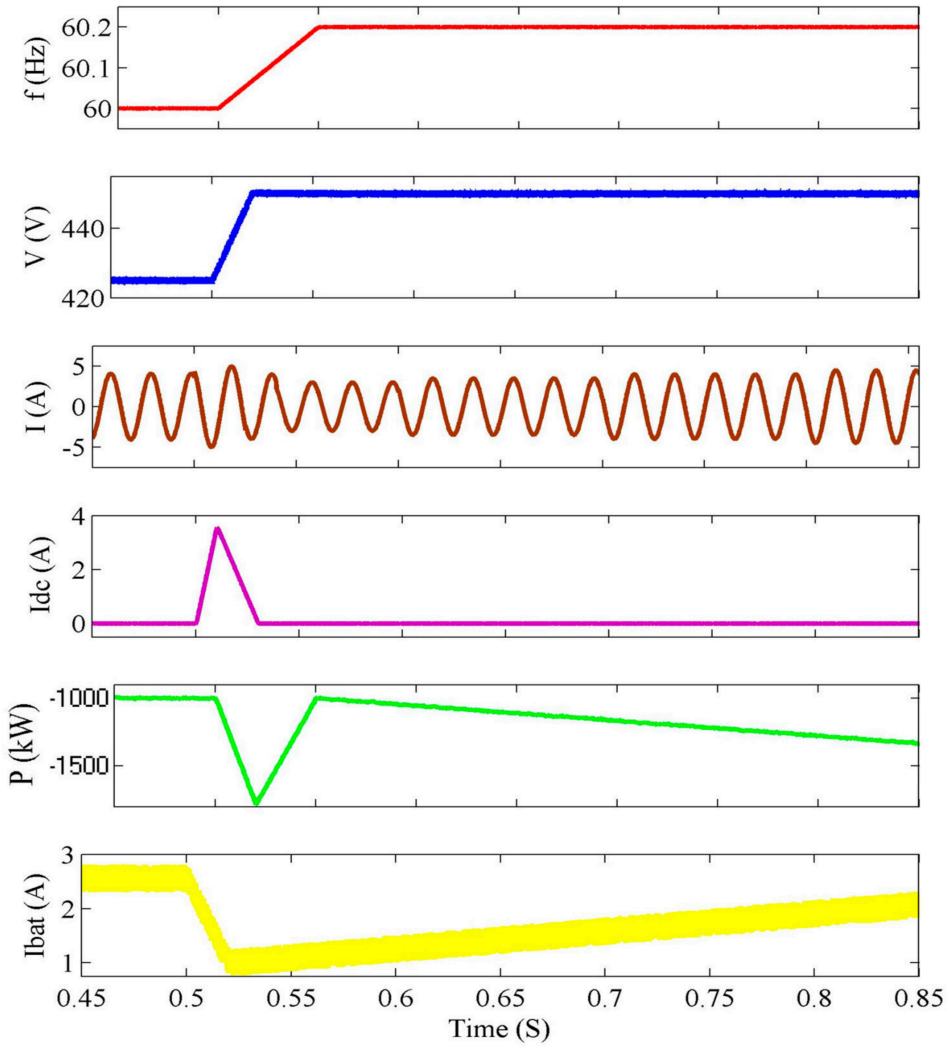


Figure 17. Main waveforms of system response for a step of +0.2 Hz.

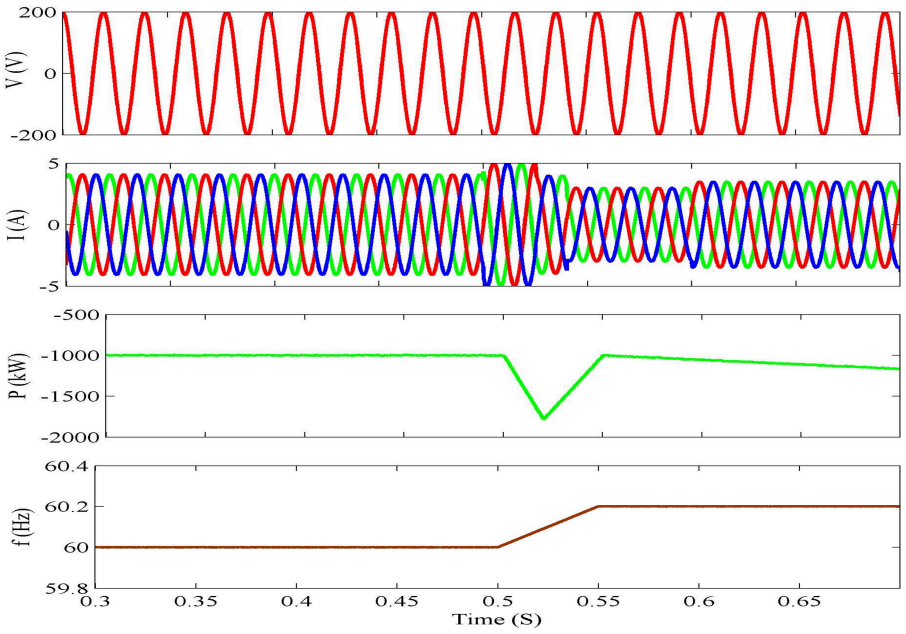


Figure 18. AC current waveforms of system response for a step of +0.2 Hz.

The VI response is validated by the transient demand of 780 W since the DC-link voltage increases from 425 to 450 V, whereas the slower dynamic response for long-term frequency support is validated by the smooth variation from −1.1 to −1.5 kW. Note that the current of DC-link capacitors achieves its steady state 80 ms after the frequency event, whereas the battery current achieves its steady state after almost s, which means 12.5 times slower than the VI controller response. Next, a step of −0.2 Hz is applied, as shown in Figures 19 and 20. The VI response is validated by the power transient of 760 W to decrease the DC-link voltage from 450 to 425 V. The slower dynamic response of active power is validated by the smooth variation of 400 W after 1 s. The results confirm that VI support is provided by DC-link capacitors whereas long-term frequency support with a slower dynamic is provided by batteries.

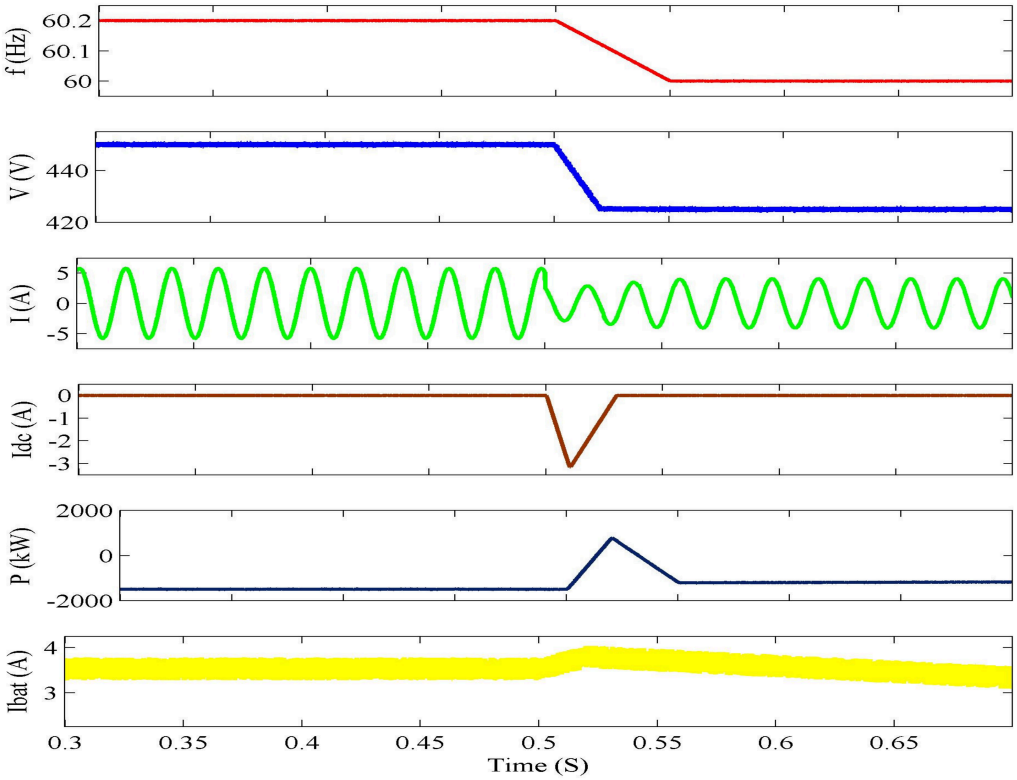


Figure 19. Main waveforms of system response for a step of −0.2 Hz.

6.4. Voltage Support by Reactive Power

Main results of the voltage support in front of a grid voltage amplitude reduction are presented in Figure 21. Amplitude decreases linearly from 179 to 162 V (17 V) in 100 ms, producing a small decrease in the -link voltage, whereas the grid current increases from 4.09 to 4.53 A (peak). According to the voltage droop controller, since reactive power increases from 0 to +400 VAR, the grid current increases from 4.53 to 4.81 A (peak) after almost 673 ms. Note that the battery current remains constant at 2.56 A. In contrast, the DC-link capacitor current is slightly increased to supply reactive power support, validating the proposed control strategy to manage the HESS. The proposed control strategy is briefly compared with similar studies implementing VI and with experimental results, which are shown in Abo-Khalil Table 5. Four comparison parameters were considered: validated V2G functionalities, control strategy, power stage configuration, and adopted energy storage devices.

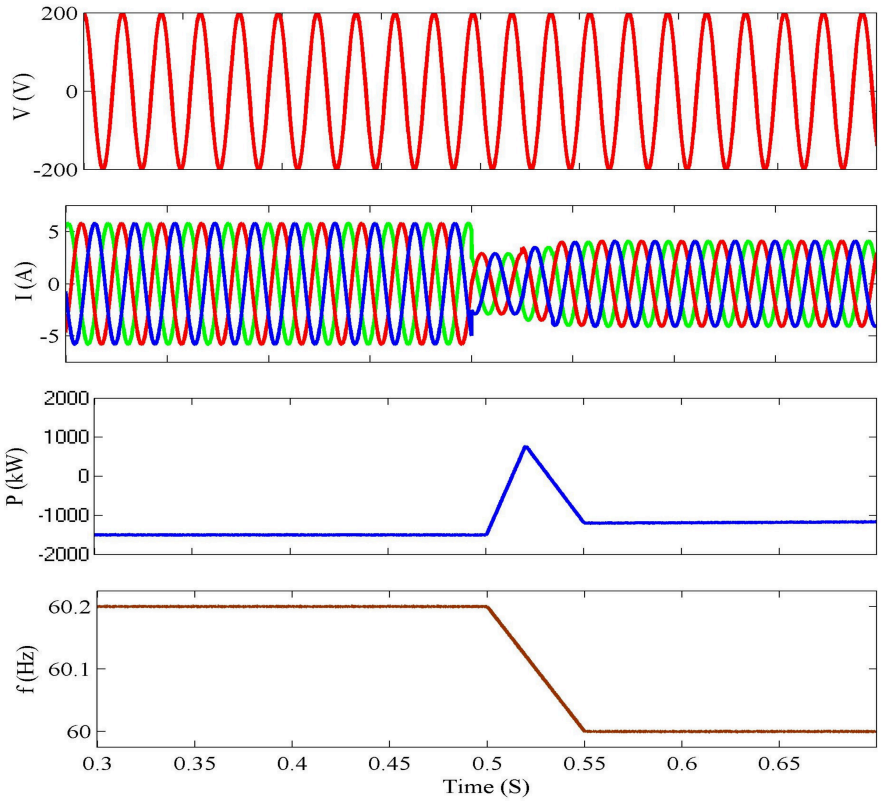


Figure 20. AC current waveforms of system response for a step of −0.2 Hz.

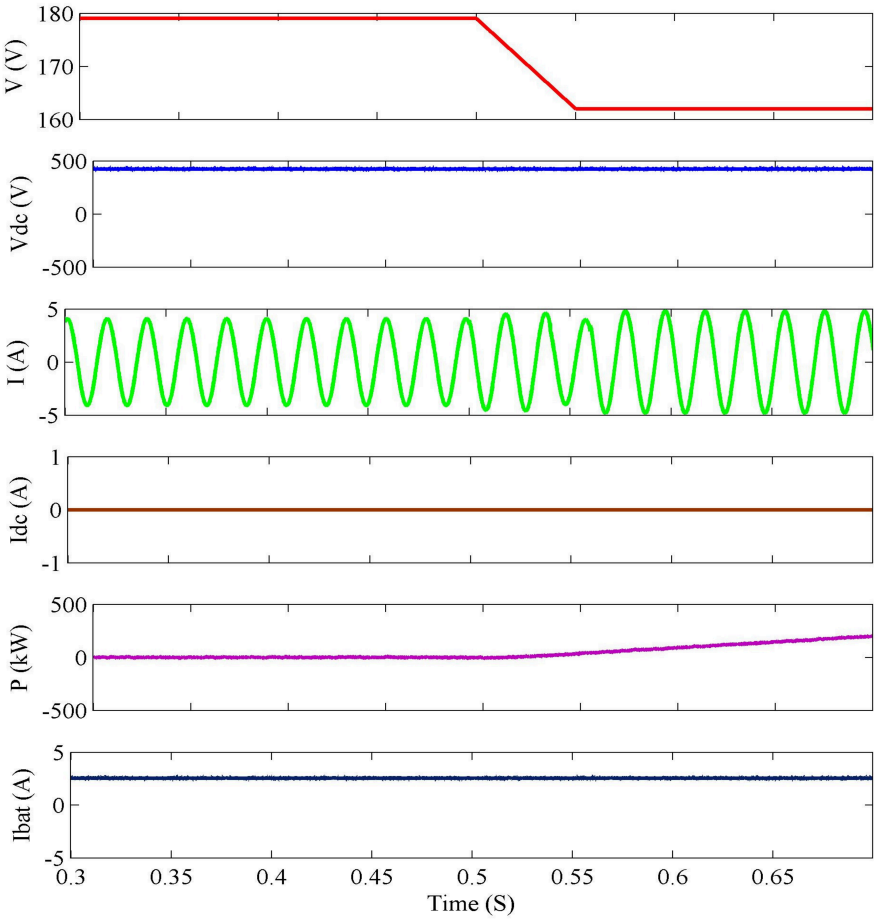


Figure 21. RPC response for an amplitude variation of −17 V.

Table 5. Comparison with existing work.

Parameter	Proposed Work	GFL Works [15,30]	GFM Works [2]	Mixed GFM and GFL Work [1]
Validated V2G Functionalities	VI, long-term frequency support, voltage support by reactive power, harmonic compensation	VI Only	VI, long-term frequency support	VI, long-term frequency support
Control Strategy	GFL	GFL	GFM	GFM for VI and GFL for long-term frequency support
Power Stage Configurations	VSI cascaded to an isolated and bidirectional DAB DC-DC converter	VSI Only	VSI cascaded to a non-isolated bidirectional Boost Converter	Two independent two-stage AC-DC converters composed of a VSI cascaded to a non-isolated bidirectional Boost Converter
Energy Storage Devices	HESS-DC-link capacitors along with battery	DC-Link Capacitors	HESS-DC-link capacitors along with battery	HESS-super capacitors along with battery

Table 6 summarizes the principal performance indicators obtained from the simulation studies. The results demonstrate that the proposed EVBC-HESS architecture effectively combines virtual inertia emulation, long-term frequency support, reactive power compensation, and harmonic mitigation within a unified control framework. The numerical values confirm the capability of the proposed system to improve grid stability and power quality while maintaining limited battery stress through coordinated energy management between the DC-link capacitor and the battery.

Table 6. Summary of key performance indicators of the proposed EVBC-HESS control strategy.

Performance Metric	Test Condition	Obtained Result
Rated Converter Power	Nominal operation	2.5 kW
Maximum Virtual Inertia Support Power	Frequency step of +0.2 Hz	786 W
Virtual Inertia Response Time	Frequency disturbance	80 ms
Long-Term Frequency Support	Frequency deviation ±0.2 Hz	±400 W
Frequency Estimation Overshoot (PLL only)	0.2 Hz frequency step	7%
Frequency Estimation Overshoot (PLL + LPF)	0.2 Hz frequency step	0.4%
Supported Frequency Variation	Grid frequency event	±0.2 Hz
Maximum Considered ROCOF	Grid code condition	3 Hz/s
Equivalent Virtual Inertia Constant	Calculated value	1.85 s
Grid Current THD	After harmonic compensation	1.50%
Grid Voltage THD	After compensation	3.23%
THDv Before Compensation	Distorted grid condition	3.19%
Reactive Power Support	Voltage sag event	+400 VAR

Table 6. *Cont.*

Performance Metric	Test Condition	Obtained Result
Grid Voltage Reduction Tested	Voltage support test	17 V
Grid Current Increase During Voltage Support	Voltage sag compensation	4.09 A → 4.81 A
Battery Current During VI Support	Frequency event	Approximately constant at 2.56 A
DC-Link Voltage Variation	Virtual inertia operation	425 V → 450 V

The quantitative comparison presented in Table 7 demonstrates that the proposed EVBC-HESS architecture provides a broader set of grid-support functionalities than existing virtual inertia implementations. In addition to delivering an equivalent virtual inertia constant of approximately 1.85 s and a transient support power of 786 W within 80 ms, the proposed system simultaneously offers long-term frequency regulation, reactive power compensation, and harmonic mitigation. The achieved current THD of 1.50% and voltage THD of 3.23% further demonstrate the capability of the proposed controller to enhance power quality while supporting grid stability. These features distinguish the proposed approach from existing studies that primarily focus on inertia emulation alone.

Table 7. Quantitative performance comparison with existing literature.

Performance Metric	Proposed Work	Ref. [15]	Ref. [2]	Ref. [1]
Virtual Inertia Support	Yes	Yes	Yes	Yes
Long-Term Frequency Support	Yes	No	Yes	Yes
Reactive Power Support	Yes (400 VAR)	No	No	No
Harmonic Compensation	Yes	No	No	No
Energy Storage Technology	DC-Link Capacitor + Battery	DC-Link Capacitor	DC-Link Capacitor + Battery	Supercapacitor + Battery
Converter Topology	VSI + Isolated DAB	VSI	VSI + Bidirectional Boost	Dual AC–DC Converters
Virtual Inertia Constant	1.85 s	N/R	N/R	N/R
Maximum Inertial Support Power	786 W	N/R	N/R	N/R
Response Time	80 ms	N/R	N/R	N/R
Maximum ROCOF Capability	3 Hz/s	N/R	N/R	N/R
Frequency Variation Tested	±0.2 Hz	N/R	N/R	N/R
Grid Current THD	1.50%	N/R	N/R	N/R
Grid Voltage THD	3.23%	N/R	N/R	N/R
Reactive Power Capability	±400 VAR	N/R	N/R	N/R
Battery Current Regulation	Yes	No	Partial	Yes
Full V2G Functionalities	Yes	Partial	Partial	Partial

Note: N/R denotes "Not Reported" in the corresponding reference.

6.5. Extension of the Proposed Strategy to IPT-Based EV Charging Systems

Recent advancements in Inductive Power Transfer (IPT) technology have enabled wireless charging solutions for electric vehicles, offering enhanced user convenience, galvanic isolation, and suitability for autonomous transportation systems. Unlike conventional conductive chargers that directly transfer electrical energy through wired connections, IPT

systems employ magnetic coupling between transmitter and receiver coils through resonant compensation networks. Consequently, IPT architecture exhibits additional dynamic characteristics associated with coupling coefficient variations, coil misalignment, resonant tuning, and power transfer efficiency.

Despite these differences, the proposed hybrid energy storage-based virtual inertia control strategy can be extended to IPT-enabled charging systems. Since the virtual inertia, frequency support, reactive power compensation, and harmonic mitigation functionalities are primarily implemented at the grid-side converter interface, the wireless power transfer stage can be treated as an intermediate energy transfer subsystem. The hybrid energy storage system comprising the DC-link capacitor and EV battery can continue to provide fast and slow frequency support services while maintaining the operational principles presented in this work. However, additional control considerations may be required to compensate for wireless coupling variations and maintain stable bidirectional power flow during V2G operation. Therefore, future work will investigate the integration of the proposed control framework with bidirectional IPT architectures to enable wireless V2G services and enhanced grid-support capabilities.

7. Conclusions

This paper presented an integrated control strategy for Electric Vehicle Battery Chargers (EVBCs) equipped with a hybrid energy storage system (HESS) consisting of a DC-link capacitor and a lithium-ion battery. The proposed architecture combines a three-phase Voltage Source Inverter (VSI) and an isolated Dual Active Bridge (DAB) converter to provide comprehensive Vehicle-to-Grid (V2G) services, including virtual inertia emulation, long-term frequency regulation, reactive power support, and harmonic compensation.

The proposed multi-timescale control framework successfully decouples fast and slow grid-support functionalities by utilizing the DC-link capacitor for transient virtual inertia response and the battery for sustained frequency support. Simulation results demonstrated that the proposed system can effectively respond to frequency disturbances of ± 0.2 Hz while maintaining stable operation. The virtual inertia controller delivered a transient support power of approximately 786 W with a response time of about 80 ms, while the equivalent virtual inertia constant achieved was approximately 1.85 s. Furthermore, the enhanced PLL-LPF frequency estimation method significantly reduced the ROCOF overshoot from approximately 7% to 0.4%, thereby improving dynamic stability and reducing transient stress on the converter system.

The harmonic compensation capability of the proposed controller was validated through FFT analysis. The grid current THD was reduced to 1.50%, while the compensated voltage THD was maintained at 3.23%, demonstrating compliance with power quality requirements and confirming the effectiveness of the selective harmonic compensation strategy. In addition, the voltage support functionality was verified under a grid voltage reduction of 17 V, where the controller supplied up to 400 VAR of reactive power support, increasing the grid current from 4.09 A to 4.81 A while maintaining an almost constant battery current of 2.56 A. These results confirm the ability of the HESS management strategy to support voltage regulation without imposing significant additional stress on the battery.

Compared with existing virtual inertia and V2G solutions, the proposed approach provides a unified framework capable of simultaneously delivering virtual inertia support, long-term frequency regulation, reactive power compensation, and harmonic mitigation using a single coordinated control architecture. The utilization of the DC-link capacitor for fast transient support reduces battery cycling stress and potentially contributes to longer battery lifetime. Furthermore, the proposed solution can be implemented as a firmware-level enhancement to existing EV charging infrastructure, facilitating cost-effective deployment

in future smart grids with high renewable energy penetration. Future work will focus on experimental validation using a hardware prototype, real-time controller implementation, scalability assessment under large-scale EV aggregation scenarios, and the extension of the proposed framework to bidirectional wireless charging and Inductive Power Transfer (IPT)-based Vehicle-to-Grid systems.

Author Contributions: Conceptualization, C.B.G., P.S.V., M.K.K. and K.V.G.R.; methodology, E.S.P.; software, C.R.R.; validation, C.B.G., P.S.V., M.K.K. and K.V.G.R.; formal analysis, E.S.P.; investigation, C.R.R.; resources, J.H.C.; data curation, C.B.G.; writing—original draft preparation, C.B.G.; writing—review and editing, C.R.R.; visualization, E.S.P.; supervision, J.H.C.; project administration, C.R.R.; funding acquisition, J.H.C. All authors have read and agreed to the published version of the manuscript.

Funding: This research received no external funding.

Data Availability Statement: The original contributions presented in this study are included in the article material. Further inquiries can be directed to the corresponding authors.

Conflicts of Interest: The authors declare no conflicts of interest.

Nomenclature

Abbreviation	Description	
EV	Electric Vehicle	
EVBC	Electric Vehicle Battery Charger	
V2G	Vehicle-to-Grid	
HESS	Hybrid Energy Storage System	
VSI	Voltage Source Inverter	
DAB	Dual Active Bridge	
PLL	Phase-Locked Loop	
LPF	Low-Pass Filter	
ROCOF	Rate-of-Change-of-Frequency	
PCC	Point of Common Coupling	
FFT	Fast Fourier Transform	
THD	Total Harmonic Distortion	
PI	Proportional–Integral	
PR	Proportional–Resonant	
RES	Renewable Energy Sources	
Symbol	Description	Unit
(f_g)	Grid frequency	Hz
(f_n)	Nominal grid frequency	Hz
(\Delta f)	Frequency deviation	Hz
(\omega_g)	Grid angular frequency	rad/s
(\Delta\omega)	Angular frequency deviation	rad/s
(P)	Active power	W
(Q)	Reactive power	VAR
(P^*)	Active power reference	W
(Q^*)	Reactive power reference	VAR
(V_{DC})	DC-link voltage	V
(V_{DC}^{*})	DC-link voltage reference	V
(C_{DC})	DC-link capacitance	F
(I_b)	Battery current	A

(V_b)	Battery voltage	V
(I_g)	Grid current	A
(V_g)	Grid voltage	V
(H_V)	Virtual inertia constant	s
(K_{VI})	Virtual inertia gain	–
(K_{\omega})	Frequency-to-voltage gain	V/Hz
(K_{dP})	Active power droop coefficient	W/Hz
(K_{dQ})	Reactive power droop coefficient	VAR/V
(P_{VI})	Virtual inertia support power	W
(P_B)	Battery support power	W
(SOC)	Battery state of charge	%
(T_s)	Sampling period	s
Subscript	**Meaning**	
g	Grid	
b	Battery	
DC	DC link	
VI	Virtual inertia	
ref (*)	Reference value	
PCC	Point of common coupling	
max	Maximum value	
min	Minimum value	
nom	Nominal value	
est	Estimated value	
LPF	Low-pass-filtered quantity	
Superscript	**Meaning**	
*	Reference value	
ˆ	Estimated quantity	
max	Maximum allowable value	
min	Minimum allowable value	
nom	Nominal operating value	

References

1. Liu, H.; Sun, C.; Zhang, X.; Wang, N.; Wang, J. Design of Energy Recovery Control for General Virtual Synchronous Machines Based on Various Forms of Energy Storage. *Appl. Sci.* **2023**, *13*, 8059. [CrossRef]
2. Fang, J.; Tang, Y.; Li, H.; Li, X. A Battery/Ultracapacitor Hybrid Energy Storage System for Implementing the Power Management of Virtual Synchronous Generators. *IEEE Trans. Power Electron.* **2018**, *33*, 2820–2824. [CrossRef]
3. Atawi, I.E.; Al-Shetwi, A.Q.; Magableh, A.M.; Albalawi, O.H. Recent Advances in Hybrid Energy Storage System Integrated Renewable Power Generation: Configuration, Control, Applications, and Future Directions. *Batteries* **2023**, *9*, 29. [CrossRef]
4. Wang, Y.; Li, W.; Liu, Z.; Li, L. An Energy Management Strategy for Hybrid Energy Storage System Based on Reinforcement Learning. *World Electr. Veh. J.* **2023**, *14*, 57. [CrossRef]
5. Tan, N.M.L.; Abe, T.; Akagi, H. Design and performance of a bidirectional isolated DC-DC converter for a battery energy storage system. *IEEE Trans. Power Electron.* **2012**, *27*, 1237–1248. [CrossRef]
6. Ecker, M.; Gerschler, J.B.; Vogel, J.; Käbitz, S.; Hust, F.; Dechent, P.; Sauer, D.U. Development of a lifetime prediction model for lithium-ion batteries based on extended accelerated aging test data. *J. Power Sources* **2012**, *215*, 248–257. [CrossRef]
7. Liu, D.; Li, H. A ZVS bi-directional DC-DC converter for multiple energy storage elements. *IEEE Trans. Power Electron.* **2006**, *21*, 1513–1517. [CrossRef]
8. Kollimalla, S.K.; Mishra, M.K.; Narasamma, N.L. Design and analysis of novel control strategy for battery and supercapacitor storage system. *IEEE Trans. Sustain. Energy* **2014**, *5*, 1137–1144. [CrossRef]
9. Ćuk, S.; Middlebrook, R.D. A new optimum topology switching DC-to-DC converter. In *Proceedings of the PESC Record—IEEE Annual Power Electronics Specialists Conference*; IEEE: Piscataway, NJ, USA, 2015; pp. 160–179. [CrossRef]
10. Fang, J.; Li, H.; Tang, Y.; Blaabjerg, F. On the Inertia of Future More-Electronics Power Systems. *IEEE J. Emerg. Sel. Top. Power Electron.* **2019**, *7*, 2130–2146. [CrossRef]
11. Tamrakar, U.; Shrestha, D.; Maharjan, M.; Bhattarai, B.P.; Hansen, T.M.; Tonkoski, R. Virtual inertia: Current trends and future directions. *Appl. Sci.* **2017**, *7*, 654. [CrossRef]

12. Hussein, M.M.; Senjyu, T.; Orabi, M.; Wahab, M.A.A.; Hamada, M.M. Control of a stand-alone variable speed wind energy supply system. *Appl. Sci.* **2013**, *3*, 437–456. [CrossRef]
13. Yan, R.; Saha, T.K.; Modi, N.; Al Masood, N.; Mosadeghy, M. The combined effects of high penetration of wind and PV on power system frequency response. *Appl. Energy* **2015**, *145*, 320–330. [CrossRef]
14. Poolla, B.K.; Bolognani, S.; Dorfler, F. Optimal Placement of Virtual Inertia in Power Grids. *IEEE Trans. Autom. Control* **2017**, *62*, 6209–6220. [CrossRef]
15. Fang, J.; Li, H.; Tang, Y.; Blaabjerg, F. Distributed Power System Virtual Inertia Implemented by Grid-Connected Power Converters. *IEEE Trans. Power Electron.* **2018**, *33*, 8488–8499. [CrossRef]
16. Meng, X.; Xie, D.; Lin, H.; Lin, C.; Ge, X.; Liu, Z. Dissipativity-Based Multiport Stability Root-Cause Identification and Mitigation for Solid-State Transformers. *IEEE Trans. Ind. Electron.* **2026**, *73*, 9850–9862. [CrossRef]
17. Makolo, P.; Zamora, R.; Lie, T.T. *The Role of Inertia for Grid Flexibility Under High Penetration of Variable Renewables—A Review of Challenges and Solutions*; Elsevier Ltd.: Amsterdam, The Netherlands, 2021. [CrossRef]
18. Du, W.; Tuffner, F.K.; Schneider, K.P.; Lasseter, R.H.; Xie, J.; Chen, Z.; Bhattarai, B. Modeling of Grid-Forming and Grid-Following Inverters for Dynamic Simulation of Large-Scale Distribution Systems. *IEEE Trans. Power Deliv.* **2021**, *36*, 2035–2045. [CrossRef]
19. Zhong, Q.C.; Weiss, G. Synchronverters: Inverters that mimic synchronous generators. *IEEE Trans. Ind. Electron.* **2011**, *58*, 1259–1267. [CrossRef]
20. Zhong, Q.C.; Nguyen, P.L.; Ma, Z.; Sheng, W. Self-synchronized synchronverters: Inverters without a dedicated synchronization unit. *IEEE Trans. Power Electron.* **2014**, *29*, 617–630. [CrossRef]
21. Taul, M.G.; Wang, X.; Davari, P.; Blaabjerg, F. Current Limiting Control with Enhanced Dynamics of Grid-Forming Converters during Fault Conditions. *IEEE J. Emerg. Sel. Top. Power Electron.* **2020**, *8*, 1062–1073. [CrossRef]
22. Abo-Khalil, A.G.; Sobhy, A.; Abdelkareem, M.A.; Olabi, A.G. Advancements and challenges in hybrid energy storage systems: Components, control strategies, and future directions. *Int. J. Thermofluids* **2023**, *20*, 100477. [CrossRef]
23. Babu, T.S.; Vasudevan, K.R.; Ramachandaramurthy, V.K.; Sani, S.B.; Chemud, S.; Lajim, R.M. A Comprehensive Review of Hybrid Energy Storage Systems: Converter Topologies, Control Strategies and Future Prospects. *IEEE Access* **2020**, *8*, 148702–148721. [CrossRef]
24. Schubert, C.; Hassen, W.F.; Poisl, B.; Seitz, S.; Schubert, J.; Oyarbide Usabiaga, E.; Gaudo, P.M.; Pettinger, K.-H. Hybrid Energy Storage Systems Based on Redox-Flow Batteries: Recent Developments, Challenges, and Future Perspectives. *Batteries* **2023**, *9*, 211. [CrossRef]
25. Cholidis, D.; Sifakis, N.; Savvakis, N.; Tsinarakis, G.; Kartalidis, A.; Arampatzis, G. Enhancing Port Energy Autonomy Through Hybrid Renewables and Optimized Energy Storage Management. *Energies* **2025**, *18*, 1941. [CrossRef]
26. Pratap Simha Reddy, S.V.; Kumar, M.V. A New Hybrid Energy Storage System for Electric Vehicle Drive System. *Eng. Technol. Appl. Sci. Res.* **2024**, *14*, 18855–18861. [CrossRef]
27. Jiao, Y. Hybrid Energy Storage Systems Capacity Optimization and Environmental Implication of Hybrid Energy Storage Systems in Renewable Power Systems. Doctoral Dissertation, KTH Royal Institute of Technology, Stockholm, Sweden, 2022.
28. Adeyinka, A.M.; Esan, O.C.; Ijaola, A.O.; Farayibi, P.K. Advancements in hybrid energy storage systems for enhancing renewable energy-to-grid integration. *Sustain. Energy Res.* **2024**, *11*, 26. [CrossRef]
29. Punyavathi, R.; Pandian, A.; Singh, A.R.; Bajaj, M.; Tuka, M.B.; Blazek, V. Sustainable power management in light electric vehicles with hybrid energy storage and machine learning control. *Sci. Rep.* **2024**, *14*, 5661. [CrossRef] [PubMed]
30. Peng, Q.; Fang, J.; Yang, Y.; Liu, T.; Blaabjerg, F. Maximum Virtual Inertia from DC-Link Capacitors Considering System Stability at Voltage Control Timescale. *IEEE J. Emerg. Sel. Top. Circuits Syst.* **2021**, *11*, 79–89. [CrossRef]

Disclaimer/Publisher's Note: The statements, opinions and data contained in all publications are solely those of the individual author(s) and contributor(s) and not of MDPI and/or the editor(s). MDPI and/or the editor(s) disclaim responsibility for any injury to people or property resulting from any ideas, methods, instructions or products referred to in the content.